



January 2019

Monte Carlo Methods And Inductor-Capacitor Network Models In Two Dimensional Superconducting And Magnetic Systems

Pragalv Karki

Follow this and additional works at: <https://commons.und.edu/theses>

Recommended Citation

Karki, Pragalv, "Monte Carlo Methods And Inductor-Capacitor Network Models In Two Dimensional Superconducting And Magnetic Systems" (2019). *Theses and Dissertations*. 2563.
<https://commons.und.edu/theses/2563>

This Dissertation is brought to you for free and open access by the Theses, Dissertations, and Senior Projects at UND Scholarly Commons. It has been accepted for inclusion in Theses and Dissertations by an authorized administrator of UND Scholarly Commons. For more information, please contact zeinebyousif@library.und.edu.

MONTE CARLO METHODS AND INDUCTOR-CAPACITOR
NETWORK MODELS IN TWO DIMENSIONAL
SUPERCONDUCTING AND MAGNETIC SYSTEMS

by

Pragalv Karki

B.S. in physics, Minnesota State University Moorhead, December 2012

A Dissertation

Submitted to the Graduate Faculty

of the

University of North Dakota

in partial fulfillment of the requirements

for the degree of

Doctor of Philosophy

Grand Forks, North Dakota

August

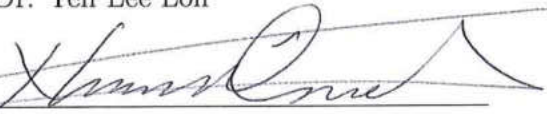
2019

Copyright 2019 Pragalv Karki

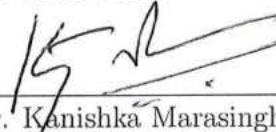
This dissertation, submitted by Pragalv Karki in partial fulfillment of the requirements for the Degree of Doctor of Philosophy from the University of North Dakota, has been read by the faculty Advisory Committee whom the work has been done and is hereby approved.



Dr. Yen Lee Loh



Dr. Nuri Oncel



Dr. Kanishka Marasinghe



Dr. William Schwalm



Dr. Mark R. Hoffmann

This dissertation is being submitted by the appointed advisory committee as having met all of the requirements of the School of Graduate Studies at the University of North Dakota and is hereby approved.



Dr. Chris Nelson,
Dean of the School of Graduate Studies

5/24/19

Date

Permission

Title Monte Carlo Methods and Inductor-Capacitor Network Models in
Two Dimensional Superconducting and Magnetic Systems.

Department Physics & Astrophysics

Degree Doctor of Philosophy

In presenting this dissertation in partial fulfillment of the requirements for a graduate degree from the University of North Dakota, I agree that the library of this University shall make it freely available for inspection. I further agree that permission for extensive copying for scholarly purposes may be granted by the professor who supervised my dissertation work or, in his absence, by the chairperson of the department or the dean of the Graduate School. It is understood that any copying or publication or other use of this dissertation or part thereof for financial gain shall not be allowed without my written permission. It is also understood that due recognition shall be given to me and to the University of North Dakota in any scholarly use which may be made of any material in my dissertation.

Pragalv Karki
June 21, 2019

TABLE OF CONTENTS

LIST OF FIGURES	ix
ACKNOWLEDGEMENTS	xiii
ABSTRACT	xv
CHAPTER	
I INTRODUCTION	1
1.1 Important developments in the history of superconductivity	1
1.2 Introduction to superconductor-insulator transition (SIT)	5
1.3 Historical background on ferromagnetism and phase transitions in ferromagnetic systems	6
II SUPERCONDUCTOR-INSULATOR TRANSITION IN INDUCTOR CAPACITOR (LC) NETWORK MODELS	8
2.1 Motivation	8
2.2 Lumped circuit element models for coarse granular superconductors	9
2.3 The LC network models	11
2.4 Leapfrog algorithm	11
2.4.1 Simple LC system	11
2.4.2 $L_{ij}C_iC_{ij}$ model	13
2.4.3 $L_{ij}C_i$ model	13
2.4.4 $L_{ij}C_{ij}$ model	14

2.5	Methods	14
2.5.1	Impulse response	14
2.5.2	Fourier transform	15
2.5.3	Window function	15
2.5.4	Rebinning	15
2.5.5	Eliminating time discretization error	16
2.5.6	Error estimation	16
2.5.7	Simulation parameters	18
2.6	Results	18
2.7	Conclusion	21
III 2D JOSEPHSON JUNCTION ARRAY		23
3.1	Motivations	23
3.2	Josephson junction	24
3.2.1	Josephson effect	25
3.2.2	Derivation of Josephson equations	25
3.2.3	Josephson coupling energy and charging energy in a Josephson junction	26
3.3	Josephson Junction Array (JJA)	27
3.3.1	JJA in a perpendicular magnetic field	28
3.4	Methods	29
3.4.1	Variational Monte Carlo (VMC)	30
3.4.2	Diffusion Monte Carlo (DMC)	31
3.4.3	Population control	33
3.4.4	VMC method for Josephson junction array	34
3.4.5	DMC method for Josephson junction array in perpendicular B field	36
3.5	Calculating observables	37

3.5.1	Energy	37
3.5.2	Magnetization	39
3.5.3	Vorticity	39
3.6	Results	40
3.7	Discussion and conclusions	46
IV	2D ANISOTROPIC ISING MODEL IN UNIAXIALLY STRAINED	
	Hf₂MnC₂O₂	49
4.1	Ising model	49
4.2	Historically important analytical solutions of 2D Ising model	50
4.2.1	Onsager's solution	50
4.2.2	Kac and Ward's approach	51
4.3	Computational method	51
4.3.1	Wolff single-cluster algorithm	52
4.3.2	Detailed balance	52
4.3.3	Ergodicity	54
4.3.4	Summary of Wolff algorithm	54
4.4	Hf ₂ MnC ₂ O ₂ MXene	55
4.5	Calculated quantities	57
4.5.1	Energy	57
4.5.2	Heat capacity	59
4.5.3	Magnetization	61
4.5.4	Susceptibility	63
4.5.5	Binder cumulant	65
4.6	Results and conclusions	65
V	SUMMARY AND DISCUSSIONS	69

APPENDICES	71
A1 Details of algorithms for LC network models	71
A1.1 Algorithm for the $L_{ij}C_iC_{ij}$ Model	71
A1.2 Algorithm for the $L_{ij}C_{ij}$ Model	72
A1.3 Maximum frequency in the $L_{ij}C_iC_{ij}$ model	74
A2 Derivation of Josephson equations	76
A3 Detailed derivations of some quantities in DMC method	77
A3.1 Expanding a term from equation (3.20)	77
A3.2 The magnetic vector potential A in a constant perpendicular B field	78
A3.3 Derivation of the drift velocity	80
REFERENCES	80

LIST OF FIGURES

2.1	<p>LC network models. A coarse granular superconductor film can be approximated by a square lattice with a fraction p of superconducting links and a fraction $1 - p$ of insulating links. In all three models, a superconducting link is represented by an inductance L_0. (a) In the $L_{ij}C_i$ model, an insulating link is represented by an open circuit, and the self-capacitance of each grain is represented by a capacitance to ground. (b) In the $L_{ij}C_{ij}$ model, an insulating link is represented by an inductance and capacitance in series. (c) The $L_{ij}C_iC_{ij}$ model combines features of the other two models, making it the most physically meaningful model.</p>	10
2.2	<p>Illustration of Verlet leapfrog algorithm for coupled differential ODEs. Variables are initialized at the beginning after which they evolve leapfrogging over each other at every other half step.</p>	11
2.3	<p>Exponent error estimation. This is a log-log plot of the dissipative conductivity $\text{Re}(\sigma)$ versus angular frequency ω of a fictitious system. The blue curve is the exact form of the trial spectrum, which contains a power law divergence $\omega^{-0.31}$ at small ω and two top hat functions. The red crosses are the extracted spectrum. The green lines are the best-fit power law. The estimate of the exponent is $a_{est} = -0.3104(1)$, as compared to the exact exponent used in the trial, $a = -0.31$. Thus, with these choices of spectral estimation and power law fitting parameters, the systematic error in a is about 0.0004. These errors are smaller than the difference between our estimates of the exponents the $L_{ij}C_i$ and $L_{ij}C_iC_{ij}$ models, which is about 0.01.</p>	17
2.4	<p>Real dynamical conductivity $\text{Re} \sigma(\omega)$ versus angular frequency for various LC network models at the percolation threshold, representing a superconductor-insulator transition. (Top) $L_{ij}C_i$ model with random $L_{ij} \in \{1, \infty\}$ and uniform $C_i = 1$, averaged over twenty 6000×6000 lattices. (Center panels) $L_{ij}C_iC_{ij}$ model with random $C_{ij} \in \{1, \infty\}$, uniform $L_{ij} = 1$, and uniform $C_i = 1, 10, 100$, averaged over twenty 6000×6000 lattices. (Bottom) $L_{ij}C_{ij}$ model with random $C_{ij} \in \{1, \infty\}$ and uniform $L_{ij} = 1$, on a 4000×4000 lattice. This is equivalent to the $L_{ij}C_iC_{ij}$ model in the limit $C_i \rightarrow 0$.</p>	19
2.5	<p>Log-log plots of $\text{Re} \sigma(\omega)$. Straight lines are power-law fits $\sigma(\omega) \propto \omega^{-a}$, with $a = 0.30408(76)$ for the $L_{ij}C_iC_{ij}$ model and $a = 0.31436(35)$ for the $L_{ij}C_i$ model. The $L_{ij}C_{ij}$ model has $a = 0$.</p>	20

3.1	Josephson junction with an insulator (INS) as the junction. A cartoon representation of Cooper pairs are shown tunneling through the INS barrier. ψ_i is the wavefunction of superconducting states and n_i is the density of Cooper pairs in the respective superconducting blocks.	24
3.2	Josephson junction array on a square lattice. The black dots represent superconducting grains and the arrows represent phases. (a) When $U \ll J$ the system is in superconducting state, and (b) when $U \gg J$ the system is in insulating state.	28
3.3	Josephson junction array in a perpendicular magnetic field. The direction of the magnetic vector potential A with respect to the magnetic field B is given by the right hand rule. The magnetization M is opposite to the applied B field since a superconductor is diamagnetic in nature, which means that the Meissner screening current j is opposite to A	29
3.4	Variational Monte Carlo (VMC) results for lattice size $L = 10$ at zero field $B = 0$. The trial energy $E_T(K)$ is minimized with respect to the variational parameter K . The green curve shows the optimal value of K . The blue curve shows E_{VMC} as a function of U/J , which is essentially a least upper bound to the true ground state energy. The red curve shows the DMC ground state energy calculated using the mixed estimator. As expected, $E_{\text{DMC}} \leq E_{\text{VMC}}$. Error bars on energies are too small to display.	35
3.5	Magnetization versus the number of time-steps in the forward walking window N_{fw} . $U = 2$, $B = 0.2$ was used for DMC calculations shown in this plot.	38
3.6	Energy (top) and magnetization (bottom) versus U/J for lattices $L = 6, 8, 10, 12$ for magnetic field $B = 0.1$, from DMC calculations with (bottom) and without (top) a guiding wavefunction. The magnetization has large error bars without a guiding wavefunction indicating that it is necessary to obtain accurate results for quantities other than energy. The inset shows the $M \sim L^4$ scaling of the magnetization in absence of an intermediate vortex state.	41
3.7	Energy (top) and magnetization (bottom) versus U/J for lattices $L = 6, 8, 10, 12$ for magnetic field $B = 0.2$. The inset shows a kink in the energy corresponding to a big drop in the magnetization caused by vortex entry as can be seen in Fig. 3.10.	42
3.8	Energy (top) and magnetization (bottom) versus U/J for lattices $L = 6, 8, 10, 12$ for magnetic field $B = 0.3$. Magnetization drop can be seen for $L = 10$ and $L = 12$ lattice around $U/J \approx 0.4$ and $U/J \approx 1$. The inset shows a kink in the energy only for $L = 10$ due to lack of space, but every magnetization drop is accompanied by a kink in the energy. Again, the drops in magnetization can be traced to a vortex entry shown in Fig. 3.10.	43

3.9	Energy (top) and magnetization (bottom) versus U/J for lattices $L = 6, 8, 10, 12$ for magnetic field $B = 0.4$. Magnetization drop can be seen for $L = 8$, $L = 10$ and $L = 12$ lattice around $U/J \approx 0.1$, $U/J \approx 0.4$ and $U/J \approx 1$. Vortex entry for these values is shown in Fig. 3.10. The magnetization scales as $M \sim L^2$ during the vortex melting.	44
3.10	Vorticity plots for lattice sizes L and magnetic fields B . Vortex formation is seen to occur mostly around $U/J \approx 0.4$ and $U/J \approx 1$ which causes abrupt drop in the magnetization and a kink in the energy. Further increasing U/J causes vortex melting. Following are U/J values going from left to right ordered in rows from top to bottom: 1st row: $U/J = 0.2, 0.5, 0.6, 0.7, 0.8, 0.9, 1, 1.1, 2, 4.5$. 2nd row: $U/J = 0.3, 1, 1.1, 1.2, 1.3, 1.4, 1.5, 1.7, 2.5, 5$. 3rd row: $U/J = 0.01, 0.1, 0.3, 0.5, 0.7, 0.9, 1, 1.5, 2, 5$. 4th row: $U/J = 0.3, 0.4, 0.5, 0.6, 0.7, 0.8, 0.9, 1.5, 3, 8.5$. 5th row: $U/J = 0.2, 0.4, 0.5, 0.6, 0.7, 0.8, 0.9, 1, 2, 3$	45
4.1	Configurations before and after a flip of a cluster (marked by the dotted lines). Red arrows represent spin up and blue arrows represent spin down. Spins immediately outside the cluster with similar orientation as the spins inside the cluster are marked with a green circle at the base and head of the arrows.	52
4.2	(a) Top and (b) side views of the $\text{Hf}_2\text{MnC}_2\text{O}_2$ monolayer with the height in z direction, and remaining two directions (x and y) in which strain is applied uniaxially.	56
4.3	(a) FM, (b) AFM1, (c) AFM2, (d) AFM3 and (e) AFM4 spin configurations with coupling J_1 and J_2 in two different directions. Only Mn atoms are considered, since contribution for magnetic moment from other atoms are negligible.	57
4.4	Energy vs. temperature for different strain values in the x direction. There is an inflection point around the Curie temperature which would correspond to a divergence in the specific heat curve in the thermodynamic limit.	58
4.5	Specific heat vs. temperature for different strain values in the x direction. Critical behavior around the Curie temperature is absent because the simulations were done on finite-sized lattices.	60
4.6	absolute Magnetization vs. temperature for different strain values in the x direction. Magnetization drops (drop becomes steeper for bigger lattice sizes and abrupt for infinitely sized lattice) to zero at the Curie temperature.	62
4.7	In a zero magnetic field, $h = 0$ the magnetization below the critical temperature can be either in a positive or negative direction as this is a spontaneous process.	63
4.8	Magnetic susceptibility vs. temperature for different strain values in the x direction. Susceptibility spikes at the Curie temperature denoting a phase transition between the ferromagnetic and paramagnetic state.	64

4.9	Binder cumulant vs. temperature for different strain values in the x direction. The crossing point at the critical point allows for an accurate extraction of the Curie temperature T_c . All the T_c values reported in this chapter are based on these Binder plots.	66
4.10	Magnetization vs. temperature for strain in both the x (a) and y (b) direction for 128×128 triangular lattices. The Curie temperature T_c is increasing with increasing strain, which can be seen in all three graphs (a), (b), and (c). (c) There is no significant difference between how T_c increases with strain in x versus y directions.	67
A.1	Magnetic vector potential in a constant perpendicular magnetic field in a symmetric gauge.	78

Acknowledgements

First and foremost I would like to thank my adviser Dr. Yen Lee Loh, who has been very kind to me throughout my graduate studies. He helped me through the problems I encountered during my dissertation projects with the utmost care and urgency. I could not have asked for a better adviser.

Next, I would like to thank my committee members Dr. Kanishka Marasinghe, Dr. Nuri Oncel, Dr. William Schwalm, and Dr. Mark R. Hoffmann for their guidance. I took several courses from Dr. Loh, Dr. Schwalm, and Dr. Oncel and I am very grateful to have had them as teachers.

Dr. Marasinghe has been tremendously helpful in all the non-academic and official works, and I cannot thank him enough because I know how extremely busy he is as the department chair and the graduate director.

I am also deeply indebted to Dr. Deniz Çakır for providing me opportunities to collaborate with him and his group to do some interesting research works that has led to fruitful results.

I would also like to thank the UND for supporting me with scholarships and assistantships, especially endowing me with the Summer Doctoral Fellowship in 2016 and helping me receive NSF ND EPSCoR DDA grant in 2018.

Finally, I cannot forget to thank all the graduate students that have been good friends to me during my stay at the UND. I would like to personally thank Dr. Rajesh Dhakal, who as my senior guided me during my early years at the UND.

I am grateful to many people I have met at the UND, as they have been very gracious and welcoming to me. I might not miss the winter too much, but I will always cherish the time I have spent here.

Dedications

I dedicate this book to my parents Bishnu Raj Karki and Mira Shah Karki, and my wife Sangeeta Shrestha. My journey to the United States to pursue education was possible only because of my parents' support. My wife has been very helpful and encouraging throughout my time as a Ph.D. student, for which I am very thankful.

ABSTRACT

The first chapter of this book provides a brief history of the important developments in superconductivity. After a general introduction, the superconductor-insulator transition is discussed in regards to open questions in the field and some of the questions tackled in this dissertation. Also, a brief introduction to ferromagnetism and phase transition in ferromagnetic systems is presented.

In the second chapter, results of simulations of three types of random inductor-capacitor (LC) networks on square lattices are presented^{1,2}. The dynamical conductivity was calculated using an equation-of-motion method. The critical exponent was extracted at low frequencies. The results suggest that there are three different universality classes and that classical percolative 2D superconductor-insulator transitions (SITs) generically have $\sigma(\omega) \rightarrow \infty$ as $\omega \rightarrow 0$.

The third chapter presents results of simulations of a quantum rotor model describing a Josephson junction array (JJA) in a perpendicular magnetic field B on a square lattice³. The SIT is tuned by the ratio of charging energy to Josephson coupling, U/J . Abrupt drops in the magnetization values were observed in the bigger lattices at certain values of B and U/J caused by the formation of vortices. Increasing U/J at a fixed B field causes quantum vortex lattice melting. The magnetization drops to zero around $U/J \simeq 5$ indicating SIT.

In the fourth chapter, results from simulations of anisotropic Ising models are presented. These simulations were performed for a $\text{Hf}_2\text{MnC}_2\text{O}_2$ monolayer under uniaxial strain⁴. The Curie temperature increases with the increasing strain, which means magnetic ordering survives up to higher temperatures under strain. In the fifth and final chapter, important results accrued over the whole dissertation are presented.

CHAPTER I

INTRODUCTION

In this chapter, some of the important developments in the history of superconductivity and phase transition in ferromagnetic systems are introduced. Chapters 2 and 3 of this dissertation concern superconductor-insulator transitions and chapter 4 focuses on phase transitions in a ferromagnetic system, so the theory of phase transitions and critical phenomena plays a central role in this dissertation.

1.1 Important developments in the history of superconductivity

The discovery of superconductivity brought a revolution in the field of condensed matter physics. Many theories that were developed to understand this new state of matter found their application in other areas of physics like nuclear and high energy physics. Following are the important developments in the understanding of this phenomenon in chronological order:

- 1911 - Heike Kamerlingh Onnes discovered superconductivity in his laboratory at Leiden University. When he was conducting experiments on the resistances of gold and mercury on 8 April 1911, he discovered the resistance of the latter to be “practically zero” at about 3 K.
- 1933 - Meissner and Ochsenfeld showed that superconductors actively expel magnetic fields, meaning that a superconductor is not only a perfect conductor

but also a perfect diamagnet⁵.

- 1935 - Fritz and Heinz London explained the electromagnetic behavior of a pure superconductor. They introduced the London equations⁶,

$$\frac{\partial \mathbf{j}_s}{\partial t} = \frac{1}{\Lambda} \mathbf{E} \quad \text{and} \quad \nabla \times \mathbf{j}_s = -\frac{1}{\Lambda} \mathbf{B},$$

where $\Lambda = m/n_s e^2$. A more meaningful constant is the penetration depth $\lambda_L = (\Lambda/\mu_0)^{1/2}$, which is the depth upto which the magnetic field penetrates the superconductor.

- 1939 - Shoenberg experimentally measured the penetration depth λ_L at Cambridge⁷.
- 1947 - Pippard developed more sensitive experiments based on microwave techniques which allowed him to investigate the effect of electron mean free path on the penetration depth⁸.
- 1950 - Maxwell and Reynolds et al. discovered the isotope effect in mercury (increasing the number of neutrons causes the superconducting critical temperature T_c to decrease)^{9,10}.
- 1950 - Based on Maxwell and Reynolds' experiments, Fröhlich made a conjecture that the electron-phonon interaction plays a crucial role in superconductivity¹¹.
- 1950 - Ginzburg and Landau developed a phenomenological theory of the phase transition from normal to superconducting state¹². Their key observation was that the phase transition in superconducting systems is of second order. They defined a complex-valued order parameter Ψ that is finite in the superconducting state and zero above the critical temperature, taking motivation from other known second-order phase transitions. The squared modulus of this pa-

parameter gives the density of superconducting “electrons” $|\Psi|^2 = n_s/2$. In the Ginzburg-Landau (GL) theory, free energy density depends only on the density of superconducting electrons $|\Psi|^2 \propto n_s$ and can be expanded in powers of $|\Psi|^2$ as,

$$F_s = F_n + \alpha|\Psi|^2 + \frac{1}{2}\beta|\Psi|^4 + \frac{1}{2m_\star} \left| \left(-i\hbar\nabla - \frac{e_\star\mathbf{A}}{c} \right) \Psi \right|^2 + \frac{1}{8\pi}(\mathbf{B}(\mathbf{r}) - \mathbf{H}_a)^2.$$

The following expression was derived for the current density from the free energy density,

$$\mathbf{j}_s = -\frac{i\hbar}{2m_\star}(\Psi^\star\nabla\Psi - \Psi\nabla\Psi^\star) - \frac{e_\star^2}{m_\star c}|\Psi|^2\mathbf{A}. \quad (1.1)$$

- 1957 - Abrikosov derived the flux-lattice solution from the GL equations showing how vortices (flux lines) emerge from the theory¹³.
- 1957 - Bardeen, Cooper, and Schrieffer published their paper explaining the microscopic theory of superconductivity which is today known as the BCS theory after their names. They showed how electrons can form Cooper pairs below the critical temperature due to the phonon-mediated net attractive interaction as conjectured by Fröhlich. Cooper pairs are bosons that can occupy the same ground state, which then facilitates the superconductivity. This is the most important breakthrough in the history of superconductivity since its discovery itself¹⁴.
- 1959 - Gorkov derived the GL equations from the BCS theory¹⁵.
- 1960 - Giaever and Nicol, Shapiro, and Smith discovered the nature of tunneling at N-S and S-S interfaces (N=Normal, S=Superconductor)^{16,17}.
- 1961 - Due to the quantum nature of the order parameter Ψ , in 1950 London predicted the quantization of magnetic flux penetrating a superconductor. Since

he did not know that the charge carriers are Cooper pairs his derived value of the flux quantum was twice the true value. The following is the derivation of flux quantization based on Bardeen's 1961 paper¹⁸. With the choice of wavefunction of $\Psi = |\Psi|e^{i\theta}$, where the phase θ is conjugate to the number (of Cooper pairs), Eq. (1.1) can be written as

$$\mathbf{j} = \frac{\hbar e}{m} |\Psi|^2 \left[\nabla\theta - \frac{2e}{\hbar c} \mathbf{A} \right].$$

Integrating the above equation along the path enclosing the magnetic flux gives

$$\oint \frac{\mathbf{j}}{|\Psi|^2} d\mathbf{l} = \frac{\hbar e}{m} \left[\oint \nabla\theta d\mathbf{l} - \frac{2e}{\hbar c} \oint \mathbf{A} d\mathbf{l} \right].$$

The first contour integral enclosing the vortex is zero because the current in the bulk of a superconductor is zero $\mathbf{j} = \vec{0}$. $\oint \nabla\theta d\mathbf{l} = 2\pi n$ because the phase must be single-valued modulo 2π , which means its gradient around a closed loop must be an integer multiple of 2π . The last contour integral is simply the magnetic flux, $\oint \mathbf{A} d\mathbf{l} = \int \mathbf{B} d\mathbf{S} = \Phi$. Putting these terms together gives

$$\Phi = n\Phi_0 \quad \text{where} \quad \Phi_0 = \frac{\pi\hbar c}{e} \approx 2.07 \times 10^{-15} \text{Wb}.$$

Φ_0 is known as the magnetic flux quantum.

- 1962 - Josephson explained the nature of Cooper pair tunneling through oxide layers separating superconductors as measured in the experiments of Giaever¹⁹.

Many more important developments have taken place in the field of superconductivity since 1962, most important being the discovery of high- T_c superconductivity in cuprates and ceramic superconductors. These high- T_c superconductors cannot be explained by the BCS theory and a lot of research today is focused on understanding the theory behind these new class of superconductors. However, in the context of this

dissertation, the Josephson pair tunneling theory in 1962 is a good stopping point in the history of superconductivity. Chapter 3 includes a detailed explanation about this tunneling phenomenon, as the chapter itself is about Josephson junction arrays.

Today, superconductivity is a big field of study within the subject of condensed matter physics. Even the study of phase transitions between superconducting, metallic, and insulating states is a big area of research. Since the research work described in chapter 2 and chapter 3 of this dissertation concerns the superconductor-insulator transition (SIT), some background on SIT is provided in the following section.

1.2 Introduction to superconductor-insulator transition (SIT)

The superconductor-insulator transition (SIT) is an incredibly interesting example of a quantum phase transition. It is called a quantum phase transition because it occurs entirely at zero temperature due to quantum mechanical fluctuations. Such a transition can be driven by different tuning parameters like disorder, magnetic field^{20,21}, thickness²², or gate voltage^{23,24}. In the recent three decades, many systems have been discovered where the superconducting state transitions into the insulating state but there are still many unanswered questions about the nature of this transition.

What universality class or classes does this transition fall in? Is the nature of the insulator bosonic or fermionic? Is it an Anderson insulator or a Mott insulator? How does the dynamical conductivity behave near the SIT? How do vortices behave under quantum mechanical fluctuations? Also, in the presence of a magnetic field B , the SIT has been shown to be of first order or second order depending on the value of the B field²⁵, further demonstrating the complex nature of this phase transition.

We have answered some of these questions in our research. In chapter 2, the nature of the dynamical conductivity near the critical point in a classical percolative SIT, driven by quenched disorder is discussed. We also identify three universality classes in the classical regime. In chapter 3 we study vortices in Josephson junction arrays

and identify the SIT by the criterion where the Meissner screening current goes to zero. Also, vortex delocalization is observed when increasing the tuning parameter that controls the strength of quantum mechanical fluctuations.

The fourth chapter is on ferromagnetic transitions in a MXene monolayer. Following section provides a brief background on the important developments in the theory of ferromagnetism.

1.3 Historical background on ferromagnetism and phase transitions in ferromagnetic systems

In 1895, French physicist Pierre Curie discovered that ferromagnetic materials become spontaneously magnetized below the critical temperature T_c , named the Curie temperature in his honor. In 1907, Pierre Weiss proposed a theoretical model based on a mean-field approach to explain such a phase transition, but his theory was unable to explain the detailed behavior of magnetization $M(T)$ near T_c as observed in the experiments. In 1920, German physicist Wilhelm Lenz proposed a model of the ferromagnetic system with spins $S_z = \pm 1$, that facilitated the parallel and anti-parallel interactions between the nearest neighbor spins²⁶. However, Lenz did not study the properties of his model in detail. He later suggested further investigation of this model as a dissertation subject for his Ph.D. student Ernst Ising.

Ising found an analytical solution to the problem in one dimension (which led to the model being named after him), which did not exhibit any phase transition. He then assumed that this model does not have any phase transitions in higher dimensions either²⁷. This was later found to be untrue. In 1936, Rudolf Ernst Peierls provided a simple argument about the possibility of spontaneous magnetization in 2D and 3D²⁸. In 1941, Hendrik Kramers and Gregory Wannier derived a quantitative result using a duality transformation that demonstrated a phase transition in 2D.

Using this method they were able to calculate the Curie temperature of the Ising model on a square lattice accurately^{29,30}

The Ising model has analytical solutions in 1D and 2D in the absence of an external magnetic field. However, the 2D Ising model with an external magnetic field and the 3D Ising model with and without an external magnetic field have not been solved analytically yet. In chapter 4, we are concerned with the 2D anisotropic Ising model in the absence of an external magnetic field, which we simulate using a computational method.

The most important breakthrough in theory of ferromagnetism came in 1942 at the February meeting of the New York Academy of Sciences. Lars Onsager announced an exact solution of the Ising model on a rectangular lattice in the absence of an external magnetic field. His 1944 paper on this topic is a landmark in the theory of critical phenomena³¹. Onsager's original solution via transfer matrix method is very complicated. Easier analytical methods exist today, many of which are based on the Pfaffian method developed independently by Kasteleyn³², Hurst-Green³³, and Fisher³⁴. The basic approach of these methods is to map the Ising partition function to that of a dimer model. Kasteleyn's combinatorial approach to the dimer problem is closely related to Kac and Ward's³⁵ combinatorial approach based on planar graphs, which is reviewed briefly at the beginning of chapter 4.

In chapter 4, we employ a computational approach based on a Markov chain Monte Carlo method to simulate the 2D anisotropic Ising model and extract the Curie temperatures for the MXene monolayer $\text{Hf}_2\text{MnC}_2\text{O}_2$ under uniaxial strain.

CHAPTER II

SUPERCONDUCTOR-INSULATOR TRANSITION IN INDUCTOR CAPACITOR (LC) NETWORK MODELS

2.1 Motivation

A superconductor-insulator transition (SIT) is a fascinating transition from a ground state with zero electrical resistance to one with infinite resistance. Thin films can undergo SITs driven by increasing disorder, applying magnetic field^{20,21}, increasing thickness²², or changing the gate voltage^{23,24}. The temperature dependence of the DC conductivity $\sigma(T)$ across a SIT has been studied extensively^{20-22,36-40}. Recent experiments are beginning to study the frequency dependence of the dynamical (AC) conductivity $\sigma(\omega)$, which gives complementary insight into the nature of the SIT.⁴¹⁻⁴⁵. There are various mechanisms that can give rise to a SIT:

1. **Pairbreaking:** the Cooper pairs may be destroyed by orbital magnetic fields, Zeeman fields, or Coulomb interactions, leaving behind localized electrons.⁴⁶
2. **Pair localization:** the Cooper pairs may remain intact but may be unable to flow through the system due to Coulomb blockade effects.⁴⁷
3. **Percolation:** if large ($1\mu\text{m}$ - 1mm) superconducting grains are randomly deposited on top of an insulating substrate, they will eventually form a connected

path through the system, changing its overall behavior from insulating to superconducting.

Previously, it was thought that the dynamical conductivity tends to a constant at low frequencies, $\sigma(\omega) \rightarrow \sigma^*$ as $\omega \rightarrow 0$, for all two-dimensional (2D) SITs.⁴⁷⁻⁶¹ However, recent numerical work suggests that at a 2D classical percolative SIT, governed by mechanism (3) above, $\sigma(\omega)$ may *diverge* as a power law $\sigma(\omega) \propto \omega^{-a}$ ($a \approx 0.3$) as $\omega \rightarrow 0$.⁶² **In this chapter, we present evidence that a divergent $\sigma(\omega)$ is indeed the norm for 2D classical percolation, rather than the exception.**^{1,2}

2.2 Lumped circuit element models for coarse granular superconductors

At low temperature $k_B T \ll T_c$, low frequencies $\hbar\omega \ll \Delta$, and small current densities, a superconducting wire of length l and cross-sectional area A behaves like an inductor of inductance $L = \frac{m_* l}{n q_*^2 A}$; it obeys the current-voltage relation $V = L\dot{I}$. In the linear response regime, a Josephson junction between two superconducting grains of critical current I_c also behaves like an inductor with $L = \frac{\hbar}{2eI_c}$. Conversely, an insulating barrier of permittivity ϵ , thickness d , and cross-sectional area A between two superconducting grains behaves like a capacitor of capacitance $C = \frac{\epsilon A}{d}$, with current-voltage relation $I = C\dot{V}$. This suggests that a coarse-grained superconductor-insulator composite can be modeled by a random inductor-capacitor (LC) network. There are many plausible ways to arrange the inductors and capacitors. Some criteria are as follows:

- A superconducting wire, or a superconducting weak link (Josephson junction), can be modeled by an inductance L_{SC} .
- An insulating barrier might be crudely approximated by the absence of a circuit element. However, even a vacuum barrier presents a finite capacitance of C_{INS} . Moreover, the electrons in a real insulating barrier possess inertia, which is

represented by a finite kinetic inductance L_{INS} . Thus a more realistic model should include both L_{INS} and C_{INS} in series.

- In a lumped circuit model, Kirchhoff’s current law asserts that no charge is allowed to build on any node. However, a real superconducting grain can store excess charge for a finite energy cost. This can be modeled by including capacitances C_{self} from each grain to an imaginary ground, held at zero potential.

We studied the $L_{ij}C_i$ model, which includes L_{SC} and C_{self} , the $L_{ij}C_{ij}$ model, which includes L_{SC} , L_{INS} , and C_{INS} .⁶², and the $L_{ij}C_iC_{ij}$ model, which includes all the circuit elements discussed above (L_{SC} , L_{INS} , C_{INS} , and C_{self}), and is thus “closest to reality.” See illustrations in Fig. 2.1. All three models exhibit a SIT at the bond percolation threshold ($p_c = 1/2$ for a 2D square lattice). The DC superfluid stiffness $\Upsilon(p)$ is identical for all three models because it only depends on how DC current flows through the inductances (all the capacitors block DC current). However, the AC (dynamical) conductivity $\sigma(\omega)$ shows remarkably different behavior for each model.

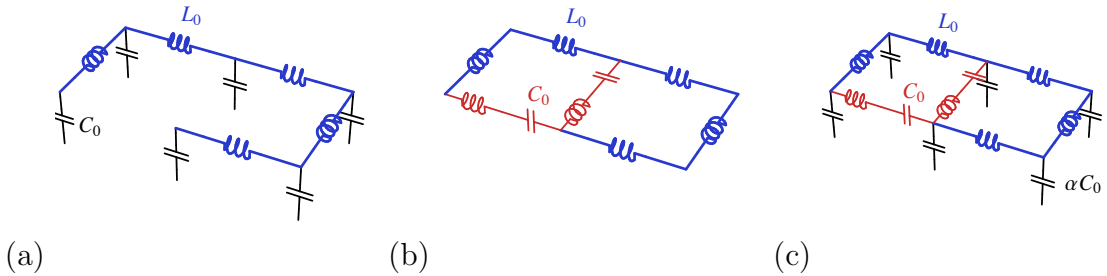


Figure 2.1: **LC network models.** A coarse granular superconductor film can be approximated by a square lattice with a fraction p of superconducting links and a fraction $1 - p$ of insulating links. In all three models, a superconducting link is represented by an inductance L_0 . (a) In the $L_{ij}C_i$ model, an insulating link is represented by an open circuit, and the self-capacitance of each grain is represented by a capacitance to ground. (b) In the $L_{ij}C_{ij}$ model, an insulating link is represented by an inductance and capacitance in series. (c) The $L_{ij}C_iC_{ij}$ model combines features of the other two models, making it the most physically meaningful model.

2.3 The LC network models

2.4 Leapfrog algorithm

We simulated the LC network models using the Verlet leapfrog algorithm which allows bigger timesteps than other methods for solving ordinary differential equations (ODEs). The error due to time-discretization can be completely removed by frequency re-mapping between the nominal frequency (frequency of the discrete-time system) and the real frequency (frequency of the original continuous-time system). The following working will illustrate that in detail.

2.4.1 Simple LC system

We first consider a system with a single harmonic oscillator mode. For a simple LC network with an inductor and a capacitor in series, the equations of motion are as follows,

$$V = \frac{1}{L} \frac{dI}{dt} \quad \text{and} \quad I = -C \frac{dV}{dt}. \quad (2.1)$$

In the Verlet leapfrog algorithm, current and voltage evolve as described in Fig. 2.2 and the following equations,

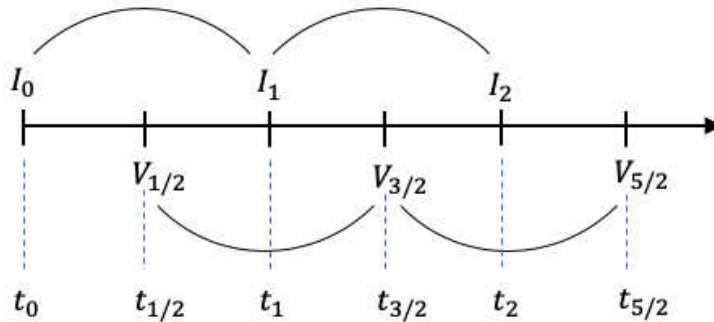


Figure 2.2: Illustration of Verlet leapfrog algorithm for coupled differential ODEs. Variables are initialized at the beginning after which they evolve leap-frogging over each other at every other half step.

$$I_{n+1} = I_n + \frac{\tau}{L} V_{n+\frac{1}{2}} \quad (2.2)$$

$$V_{n+\frac{1}{2}} = V_{n-\frac{1}{2}} - \frac{\tau}{C} I_n \quad (2.3)$$

$$V_n = \frac{1}{2} \left(V_{n+\frac{1}{2}} + V_{n-\frac{1}{2}} \right). \quad (2.4)$$

This gives the discrete version of the second order differential equation as

$$I_{n-1} + \left(\frac{\tau^2}{LC} - 2 \right) I_n + I_{n+1} = 0 \quad (2.5)$$

with solution

$$I_n = Ae^{i\lambda n} + Be^{-i\lambda n}. \quad (2.6)$$

Then substituting the expressions for I_n , I_{n+1} and I_{n-1} according the Eq. (2.6) into the Eq. (2.5) gives

$$I_n = 2A \left[\frac{2}{\tau} \left(\sin^{-1} \left(\frac{\omega\tau}{2} \right) \right) t - \frac{\pi}{2} \right] \quad (2.7)$$

where, $\omega = 1/\sqrt{LC}$ is the true frequency of the circuit. The current oscillates at a nominal frequency Ω as

$$\Omega = \frac{2}{\tau} \sin^{-1} \left(\frac{\omega\tau}{2} \right). \quad (2.8)$$

If $\tau > 2/\omega$ then Ω is imaginary and the leapfrog algorithm is unstable. Thus, the largest acceptable time-step τ_{\max} is dictated by the highest eigenmode frequency ω_{\max} .

In a more complicated linear system, even if we do not know the eigenmodes explicitly, we know that the eigenmodes evolves independently at its “nominal frequency” (according to the leapfrog algorithm). This allows us to eliminate the errors due to time discretization by mapping nominal frequencies back to the true frequencies (see section 2.5.5)

2.4.2 $L_{ij}C_iC_{ij}$ model

For the $L_{ij}C_iC_{ij}$ model [Fig. 2.1(c)], Kirchoff's junction rule gives the following equations of motion:

$$\dot{V}_i = \frac{1}{C_i} \sum_{j@i} I_{ij} \quad (2.9)$$

$$\dot{U}_{ij} = \frac{1}{C_{ij}} I_{ij} \quad (2.10)$$

$$\dot{I}_{ij} = \frac{1}{L_{ij}} (V_i - V_j - U_{ij}), \quad (2.11)$$

where C_i is the self-capacitance of grain i , $j@i$ means that j runs over all neighbors of i , C_{ij} and L_{ij} are the capacitance and inductance along bond ij , V_i is the potential on grain i , I_{ij} is the current along bond ij , and U_{ij} is the voltage across the capacitance C_{ij} . All inductances are identical ($L_{ij} = L$) and all capacitances-to-ground are identical ($C_i = C_1$). Bond capacitances are chosen randomly with values C_2 and ∞ :

$$C_{ij} = \begin{cases} \infty & \text{with probability } p \\ C_2 & \text{with probability } 1 - p. \end{cases} \quad (2.12)$$

We set $L = 1$ and $C_2 = 1$, and we do calculations for many values of C_1 . We focus on the case $p = 0.5$, exactly at the bond percolation threshold.

The dynamical conductivity is defined as $\sigma(\omega) = J_x(\omega)/E_x(\omega)$, where J_x is the current density induced by an applied electric field E_x oscillating at frequency ω . Details of how the leapfrog algorithm is applied to this model are given in Appendix A1.1.

2.4.3 $L_{ij}C_i$ model

In the limit $C_{ij} \rightarrow \infty$, Eq. (2.10) gives $U_{ij} = 0$, and Eq. (2.11) becomes $\dot{I}_{ij} = \frac{1}{L_{ij}} (V_i - V_j)$. The leapfrog algorithm for this model is a special case of the general

algorithm for the $L_{ij}C_iC_{ij}$ model⁶².

2.4.4 $L_{ij}C_{ij}$ model

In the limit $C_i \rightarrow 0$, Eq. (2.9) reduces to Kirchhoff’s junction rule, $\sum_{j@i} I_{ij} = 0$. However, there are some challenges in adapting the leapfrog method to the $L_{ij}C_{ij}$ model. As $C_i \rightarrow 0$, the excitation spectrum splits into low-frequency modes whose current patterns avoid the on-site capacitors, and high-frequency modes involving large currents through the on-site capacitors. Thus Eq. (2.9) becomes stiff and requires a small time step $\tau \ll 1$ to simulate. (Details are provided in Appendix A1.2)

2.5 Methods

We calculated $\text{Re } \sigma(\omega)$ using an equation-of-motion method, in which the system is stimulated with a uniform electric field pulse and the subsequent “free induction decay” signal is Fourier-transformed to give $\text{Re } \sigma(\omega)$. We imagine that a transient uniform electric field in the x direction is applied to the system. This produces a transient emf in every inductor along the x direction, and hence an initial current.

Simulations were done for $L_{ij} = C_{ij} = 1$, and $C_i = 1, 2, 3, 4, 5, 10, 100$. For $C_i = 1$ and $C_i = 100$ the maximum frequency and hence the maximum time-step for simulation to be stable are $\omega_{\text{max}} = 3$, $\tau_{\text{max}} = 0.666667$, and $\omega_{\text{max}} = 1.03923$, $\tau_{\text{max}} = 1.924501$ respectively (details in Appendix A1.3). All the simulations were performed with a time-step $\tau = 0.5$ to maintain consistency.

2.5.1 Impulse response

At each timestep we record the average current density in the x direction, $G_n = \frac{1}{N_x N_y} \sum_{xy} I_{xy}^X|_{t=n\tau}$. This time series represents the impulse response (Green function) of the discrete-time system.

2.5.2 Fourier transform

Performing a Fourier transform gives the nominal dynamical conductivity $\text{Re } \tilde{\sigma}(\tilde{\omega})$ as a function of nominal frequency $\tilde{\omega}$, $\tilde{\sigma}(\tilde{\omega}) = \sum_{n=0}^{\infty} e^{i\tilde{\omega}n\tau} G_n$. We actually use a discrete cosine transform to calculate the dissipative part of the response, $\text{Re } \tilde{\sigma}(\tilde{\omega}) = \sum_{n=0}^{\infty} (\cos \tilde{\omega}n\tau) G_n$. If desired, we can reconstruct the reactive response $\text{Im } \tilde{\sigma}$ from the dissipative response, using the Kramers-Kronig relations.

2.5.3 Window function

Since the simulation is run for a finite number of timesteps N_τ , we know G_n only for $0 \leq n < N_\tau$. Truncating the time series and performing a partial sum would lead to severe ringing (Gibbs oscillations) in the estimated spectrum. Therefore we multiply the time series by a window function before transforming: $\text{Re } \tilde{\sigma}^{\text{est}}(\tilde{\omega}) = \sum_{n=0}^{\infty} (\cos \tilde{\omega}n\tau) W_n G_n$. We choose a Kaiser window function involving the modified Bessel function I_0 , $W_n = W_{\text{Kaiser}}(x_n)$, where $W_{\text{Kaiser}}(x) = I_0(\beta\sqrt{1-x^2})/I_0(\beta)$ and $x_n = n/(N_\tau - 1)$. The width parameter $\beta = 24$ is chosen conservatively so that the spectral leakage function has a broad central lobe but falls off very quickly thereafter.⁶²

2.5.4 Rebinning

The calculation is implemented as a fast type-III discrete cosine transform (DCT), such that we obtain estimates of the spectrum at “half-integer” frequencies $\tilde{\omega} = (m + \frac{1}{2})\frac{2\pi}{\tau}$ ($m = 0, 1, 2, \dots, N_\tau - 1$). The output values of the DCT are interpreted as weights in bins, where the m th bin is $\frac{2\pi m}{\tau} < \tilde{\omega} < \frac{2\pi(m+1)}{\tau}$. The resulting raw spectrum could be plotted as a histogram with N_τ bins, but this misrepresents the frequency resolution as being higher than it actually is. With the chosen window function, the spectrum of a single LC oscillator leads to a peak spanning approximately 15

bins. Therefore, we regroup the spectral weight into $\lfloor N_\tau/15 \rfloor$ bins, in a manner that conserves the total weight. This is done by calculating the cumulative distribution function (CDF) on the fine grid, interpolating, resampling onto the coarse grid, and taking differences. A delta function in the true spectrum is spread across at most two bins in the estimated spectrum.

2.5.5 Eliminating time discretization error

The above calculation gives the nominal dynamical conductivity $\text{Re } \tilde{\sigma}(\tilde{\omega})$ as a function of nominal frequency $\tilde{\omega}$. The frequency error is a consequence of the time discretization in the leapfrog algorithm. This error can be removed completely by remapping the spectrum to $\text{Re } \sigma(\omega) = \frac{d\tilde{\omega}}{d\omega} \text{Re } \tilde{\sigma}(\tilde{\omega})$. (It is convenient to perform the remapping and rebinning together in one step.)

To summarize, if a system has the spectrum $G(\omega)$, then simulating it with the leapfrog algorithm with timestep τ produces the time series

$$G_n = 2 \int_0^{2/\tau} d\omega \cos(2n \arcsin \frac{\omega\tau}{2}) G(\omega), \quad n = 0, 1, 2, 3, \dots$$

The entire spectral estimation procedure serves to estimate $G(\omega)$ based on a truncated time series G_n ($n = 0, 1, 2, \dots, N_\tau$).

2.5.6 Error estimation

Typically, $\text{Re } \sigma(\omega)$ has a power-law peak at small ω . Even with the aforementioned conservative choices for windowing and rebinning, one may still be concerned that the windowing procedure may broaden the peak and modify the power law. To rule this out, we have chosen several test spectra, generated corresponding time series, fed these through the algorithm, and compared with the original spectra. As explained in a previous study,⁶² the frequency resolution (“horizontal error bar”) is $\Delta\omega \approx 10^{-3}$ and

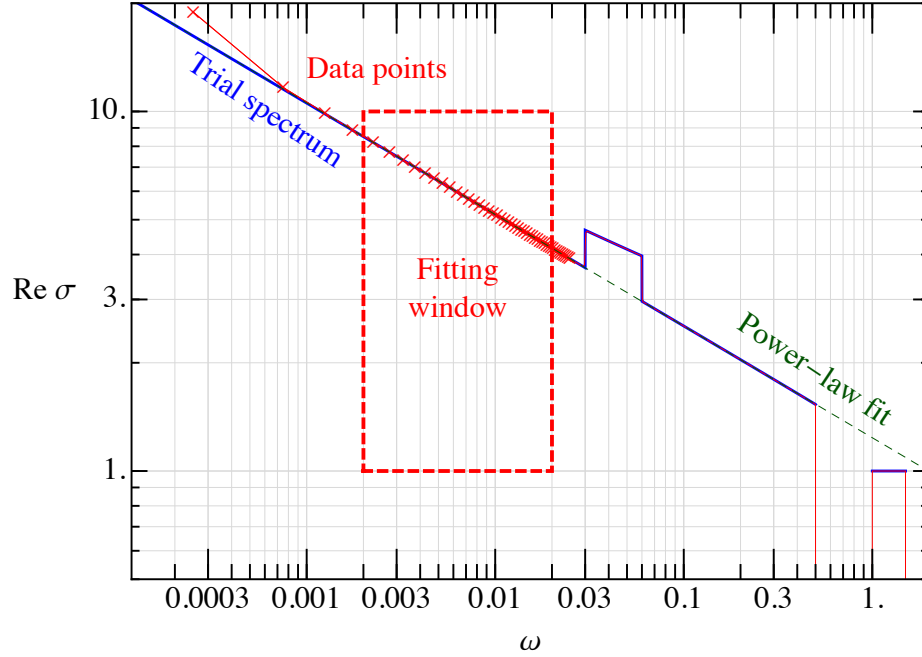


Figure 2.3: Exponent error estimation. This is a log–log plot of the dissipative conductivity $\text{Re}(\sigma)$ versus angular frequency ω of a fictitious system. The blue curve is the exact form of the trial spectrum, which contains a power law divergence $\omega^{-0.31}$ at small ω and two top hat functions. The red crosses are the extracted spectrum. The green lines are the best-fit power law. The estimate of the exponent is $a_{est} = -0.3104(1)$, as compared to the exact exponent used in the trial, $a = -0.31$. Thus, with these choices of spectral estimation and power law fitting parameters, the systematic error in a is about 0.0004. These errors are smaller than the difference between our estimates of the exponents the $L_{ij}C_i$ and $L_{ij}C_iC_{ij}$ models, which is about 0.01.

the spectral leakage (“vertical error bar”) is $\frac{\Delta\sigma}{\sigma} \approx 10^{-8}$. In order to estimate the error in the exponent of a power law fit, we generate exact time series data for a spectrum with a *known* power law, feed this into the spectral estimation code, and compare the results with the true spectrum, as illustrated in Fig. 2.3. The trial spectrum (and the corresponding time series) is a combination of the ingredients below:

$$\begin{aligned}
G^{\text{pow}}(\omega) &= \Theta(\omega_0 - \omega) (\arcsin \frac{\omega\tau}{2})^{-a} \\
G_n^{\text{pow}} &= \frac{2^a \text{Im } i^a [\Gamma(1 - a, 0) - \Gamma(1 - a, i|n + \frac{1}{2}|x)]}{\tau |n + \frac{1}{2}|^{1-a}} \\
&\quad - \frac{2^a \text{Im } i^a [\Gamma(1 - a, 0) - \Gamma(1 - a, i|n - \frac{1}{2}|x)]}{\tau |n - \frac{1}{2}|^{1-a}} \\
G^{\text{box}}(\omega) &= \Theta(\omega_0 - \omega) \\
G_n^{\text{box}} &= \Omega_0 [\text{sinc}(n + \frac{1}{2})\Omega_0 + \text{sinc}(n - \frac{1}{2})\Omega_0].
\end{aligned}$$

The results suggest that the systematic error in the exponent due to the spectral estimation procedure is $\Delta a \lesssim 0.0004$.

2.5.7 Simulation parameters

Simulations of the $L_{ij}C_iC_{ij}$ model were performed at the bond percolation threshold $p_c = 1/2$, on 6000×6000 square lattices, for $N_\tau = 60000$ timesteps, with timestep $\tau = 0.5$, for 20 different disorder realizations. Simulations were written in C++ and run on a Dell T7500 workstation with 4 cores, using OpenMP for parallelization. Each run took around 5.5 hours of wall time.

2.6 Results

Figure 2.4 shows how the conductivity spectrum $\text{Re } \sigma(\omega)$ of the $L_{ij}C_iC_{ij}$ model “interpolates” between the spectra of the $L_{ij}C_i$ and $L_{ij}C_{ij}$ models as the grain self-

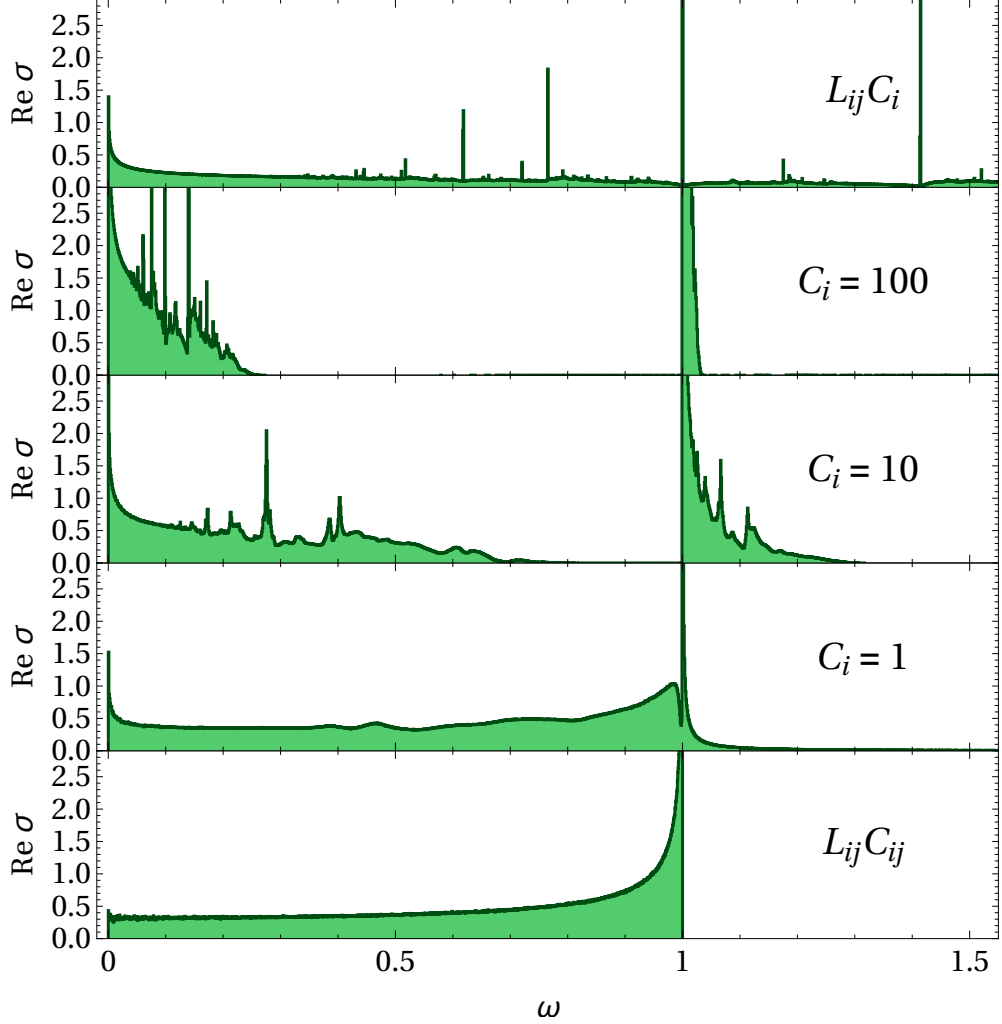


Figure 2.4: Real dynamical conductivity $\text{Re } \sigma(\omega)$ versus angular frequency for various LC network models at the percolation threshold, representing a superconductor-insulator transition. (Top) $L_{ij}C_i$ model with random $L_{ij} \in \{1, \infty\}$ and uniform $C_i = 1$, averaged over twenty 6000×6000 lattices. (Center panels) $L_{ij}C_iC_{ij}$ model with random $C_{ij} \in \{1, \infty\}$, uniform $L_{ij} = 1$, and uniform $C_i = 1, 10, 100$, averaged over twenty 6000×6000 lattices. (Bottom) $L_{ij}C_{ij}$ model with random $C_{ij} \in \{1, \infty\}$ and uniform $L_{ij} = 1$, on a 4000×4000 lattice. This is equivalent to the $L_{ij}C_iC_{ij}$ model in the limit $C_i \rightarrow 0$.

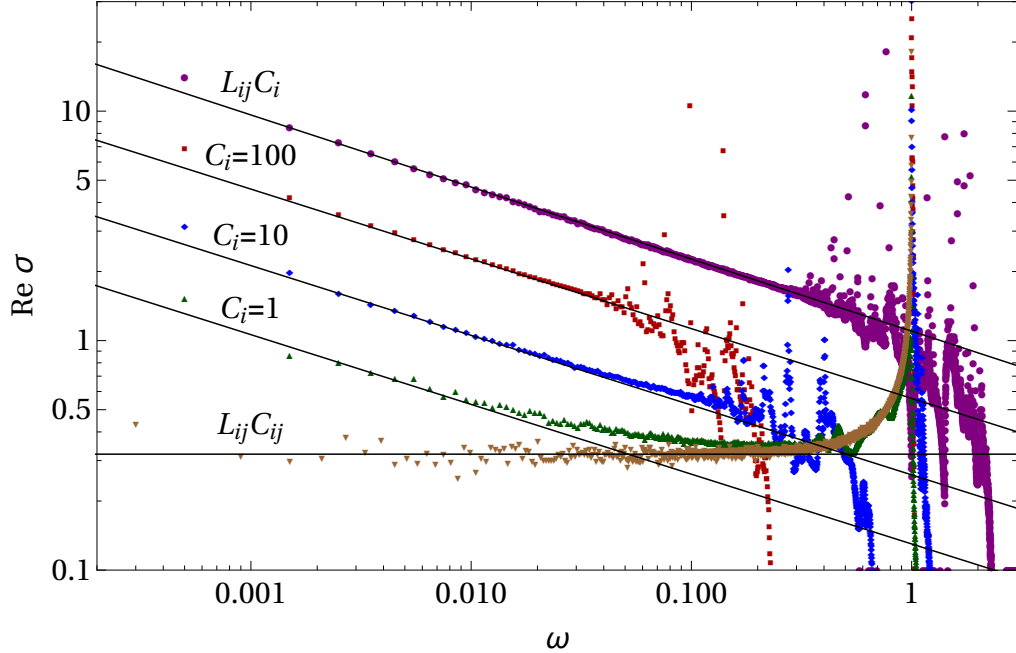


Figure 2.5: Log–log plots of $\text{Re } \sigma(\omega)$. Straight lines are power-law fits $\sigma(\omega) \propto \omega^{-a}$, with $a = 0.30408(76)$ for the $L_{ij}C_iC_{ij}$ model and $a = 0.31436(35)$ for the $L_{ij}C_i$ model. The $L_{ij}C_{ij}$ model has $a = 0$.

capacitance C_i varies.

In the limit $C_i \rightarrow 0$ the on-site capacitors become open circuits. Then the $L_{ij}C_iC_{ij}$ model [Fig. 1(c)] reduces to the $L_{ij}C_{ij}$ model [Fig. 1(b)]. The spectrum is constant at low frequencies and diverges at $\omega \rightarrow 1$, as shown in the bottom panel of Fig. 2.4.

For small on-site capacitances ($C_i = 1$), the overall spectrum remains smooth, but there are some changes near $\omega = 1$, and a power law divergence appears at low frequency. As C_i increases, this power law is more pronounced and persists over a larger frequency range. The spectrum also develops a spiky nature, and a gap opens for $C_i \gtrsim 4$. As $C_i \rightarrow \infty$, the on-site capacitors can carry large amounts of current, and one might expect that they dominate the physics, so that the system behaves more like the $L_{ij}C_i$ model [Fig. 1(a)]. However, the $L_{ij}C_iC_{ij}$ model (with random C_{ij}) may not reduce exactly to the $L_{ij}C_i$ model (with random L_{ij}).

Figure 2.5 combines all the data on a log-log plot. At large values of C_i , or at low frequencies, the spectra obey power laws of the form $\text{Re } \sigma(\omega) = b\omega^{-a}$, shown as

straight lines. The dynamical conductivity critical exponent a is the slope of the lines. It is extracted by fitting over appropriate ranges. We obtain $a = 0.30408(76)$ for the $L_{ij}C_iC_{ij}$ model and $a = 0.31436(35)$ for the $L_{ij}C_i$ model. As explained in the previous section, this estimate is subject to systematic error and random error. Nevertheless, it suggests that the two models may lie in two distinct universality classes.

2.7 Conclusion

For the three models illustrated in Fig. 2.1, the real dynamical conductivity goes as $\text{Re } \sigma \sim \omega^{-a}$ as $\omega \rightarrow 0$, but the critical exponent a appears to be different. We find $a = 0$ for the $L_{ij}C_{ij}$ model, $a = 0.304(1)$ for the $L_{ij}C_iC_{ij}$ model, and $a = 0.314(4)$ for the $L_{ij}C_i$ model. These represent three universality classes for the SIT, at least as far as dynamical conductivity is concerned. In the language of renormalization group flows, we conjecture that the $a = 0$ class is associated with a fixed point with $C_i = 0$, which is unstable with respect to the relevant parameter C_{ij} . Conversely, the $a = 0.314$ class is associated with a fixed point with $C_{ij} = 0$, which is unstable with respect to the relevant parameter C_i , and flows towards the $a = 0.304$ fixed point. In any real experiment both C_i and C_{ij} are guaranteed to be present, so we expect $a = 0.304$.

There is also the possibility of the two critical exponents which are close to each other being the same, even though the difference between them is bigger than random error and systematic error combined. The discrepancy could be due to corrections to scaling. In order to address this more definitely, one could simulate larger systems with more disorder realizations, study the different models in higher dimensions to see if the difference in exponents is more pronounced, or calculate other quantities like magnetic and electric susceptibilities as a function of p and use the critical exponent relations to extract a indirectly.

However it is more important to realize the dominance of C_i over C_{ij} . Roughly

speaking, under a reblocking transformation that groups four sites into one, we would expect that C_i grows by 4 (since the new superconducting islands are four times as large) whereas C_{ij} stays the same (for the same reason that the sheet resistance does not change under scaling). This may serve as a crude explanation of why C_i plays a much more important role than C_{ij} in controlling the critical behavior.

As remarked in the introduction, most theories of superconductor-insulator transitions⁴⁷⁻⁶¹ predict a finite conductivity, $\text{Re } \sigma(\omega) \rightarrow \sigma^*$ as $\omega \rightarrow 0$. Our work shows that 2D classical percolative SITs generically have a divergent conductivity, $\text{Re } \sigma(\omega) \rightarrow \infty$ as $\omega \rightarrow 0$.

CHAPTER III

2D JOSEPHSON JUNCTION ARRAY

3.1 Motivations

Diffusion Monte Carlo (DMC) is a projector Monte Carlo (PMC) method that has been applied to many continuum quantum systems: solid state physics^{63–71}, chemistry^{72–76}, and nuclear physics^{77,78}. Green function Monte Carlo (GFMC), which is a PMC method similar to DMC, has been used to simulate the 2D $S = 1/2$ Heisenberg antiferromagnet^{79,80}. Surprisingly, DMC itself has not been applied to any quantum lattice models so far, path-integral Monte Carlo (PIMC) being the primary choice of method^{81–85}. In this chapter, DMC is applied to a lattice model for the first time and also a comparison is made between calculations performed with and without importance sampling³.

The model in concern is the 2D Josephson junction array (JJA) Hamiltonian with on-site Coulomb interactions and nearest-neighbor Josephson couplings in the presence of a perpendicular magnetic field. There is a vast amount of literature on JJAs and related Bose-Hubbard models, including theoretical studies using mean-field theory^{86,87}, diagram methods⁸⁸, and worldline quantum Monte Carlo methods such as PIMC^{89,90}. Many experiments have been performed on lithographically fabricated JJAs^{91,92}. A 2D JJA exhibits a finite-temperature superconducting-to-normal transition in the Berezinskii-Kosterlitz-Thouless (BKT) universality class due to vortex-antivortex unbinding. It also exhibits a zero-temperature superconductor-insulator transition (SIT) tuned by the competition between Josephson energy and Coulomb

energy⁸⁶. In this study, we are concerned with the SIT at zero temperature in the presence of a perpendicular magnetic field. A SIT is a fascinating transition from a ground state with zero electrical resistance to one with infinite resistance. SITs have been extensively investigated, not only in JJAs, but also in amorphous thin films, where the SIT may be tuned by increasing disorder⁹³, applying magnetic field^{20,21}, increasing thickness²², or changing the gate voltage^{23,24}. The magnetic-field-tuned SIT may involve transitions between various types of vortex matter, such as vortex glasses, vortex lattices, and vortex liquids. The exact reasons and conditions for a transition to these different types of states are still not completely understood. A strong motivation for our study is to introduce DMC as a tool for future studies to investigate larger systems to shed more light on the nature of the field-tuned SIT.

3.2 Josephson junction

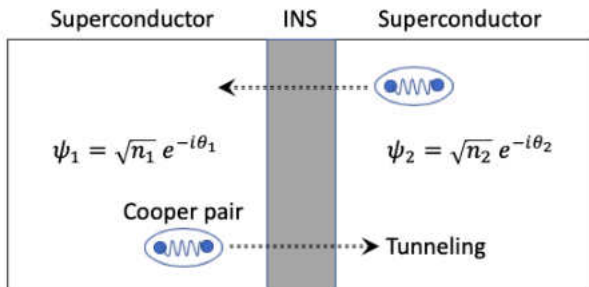


Figure 3.1: Josephson junction with an insulator (INS) as the junction. A cartoon representation of Cooper pairs are shown tunneling through the INS barrier. ψ_i is the wavefunction of superconducting states and n_i is the density of Cooper pairs in the respective superconducting blocks.

A Josephson Junction is a junction or a weak link between two superconducting materials (or grains) through which Cooper pairs can tunnel. The weak link could be an insulator⁹⁴, normal conductor⁹⁵, or superconductor with weak electrical contacts or narrow channels between superconducting grains⁹⁶. A Josephson junction with an insulating weak link (Fig 3.1) is discussed

in this section. The tunneling of Cooper pairs is called the Josephson effect and is the basis of superconducting quantum interference devices (SQUIDS)^{97,98} that are used for measuring ultrasensitive electric and magnetic fields.

3.2.1 Josephson effect

The Josephson effect is the phenomenon of Cooper pair tunneling through a junction between superconductors. The tunneling current I between superconductors is dependent on the density of Cooper pairs n_i given by the eigenvalue of the number operator \hat{n} . The voltage across the junction is related to the phase variable. The number and the phase operators satisfy the commutation relation

$$[\hat{\theta}, \hat{n}] = i\hbar.$$

In the phase representation, $\hat{n} = -i\hbar\partial/\partial\theta$ (analogous to \hat{x} and \hat{p}). The Equations describing the Josephson effect are as follows,

$$\frac{d\theta}{dt} = \frac{e_*}{\hbar}V(t) \quad \text{and} \quad I = I_c \sin \theta, \quad (3.1)$$

where $e_* = 2e$ is the charge of a Cooper pair, $V = V_1 - V_2$ is the potential difference between the superconductors, $\theta = \theta_1 - \theta_2$ is the phase difference between the superconductors, and I_c is the critical current. The critical current is the maximum current above which the superconductivity is destroyed.

3.2.2 Derivation of Josephson equations

The Josephson equations can be derived starting from the following coupled Schrödinger's equations (setting $\hbar = 1$),

$$\begin{aligned} i\frac{\partial\psi_1}{\partial t} &= U_1\psi_1 + \alpha\psi_2 \\ i\frac{\partial\psi_2}{\partial t} &= U_2\psi_2 + \alpha\psi_1, \end{aligned} \quad (3.2)$$

where $U_i = e_* V_i$ is the potential energy of each superconductor, and α is the coupling constant across the insulating barrier. Then the following substitution can be made for the wavefunction ψ_i ,

$$\psi_i = \sqrt{n_i} e^{i\theta_i}. \quad (3.3)$$

This expression for the wavefunction was introduced by Ginzburg and Landau in their phenomenological theory of phase transition in superconducting systems. Substituting Eq. (3.3) into Eq. (3.2) yields the Josephson equations in Eq. (3.1) (details in Appendix A2), with the critical current and the potential difference given by:

$$I_c = 2e_* \alpha \sqrt{n_1 n_2} \quad \text{and} \quad V = \frac{U_1 - U_2}{e_*}. \quad (3.4)$$

3.2.3 Josephson coupling energy and charging energy in a Josephson junction

There are two competing effects in a Josephson junction: (1) the Josephson coupling between phases that tends to delocalize Cooper pairs, and (2) the Coulomb blockade that tends to localize Cooper pairs on each grain.

The coupling energy E_{Jos} can be derived by noting that the power delivered between the grains is

$$\frac{dE_{\text{Jos}}}{dt} = IV = (I_c \sin \theta) \frac{\hbar}{e_*} \frac{d\theta}{dt}. \quad (3.5)$$

Integrating Eq. (3.5) yields the expression

$$E_{\text{Jos}} = -J \cos \theta, \quad (3.6)$$

where $J = \hbar I_c / e_*$ is called the Josephson energy. The Coulomb energy E_{Coul} of the

superconducting grain is given by

$$E_{\text{Coul}} = \frac{1}{2}CV^2 = \frac{Q^2}{2C} = \frac{(2en)^2}{C} = \frac{U}{2}n^2, \quad (3.7)$$

where, $U = (2e)^2/C$ is called the charging energy in the literature^{25,85}.

3.3 Josephson Junction Array (JJA)

The Hamiltonian of a Josephson junction array can be written by combining the Coulomb blockade effect and the Josephson effect,

$$\hat{H} = \frac{C}{2} \sum_i \hat{V}_i^2 - J \sum_{\langle ij \rangle} \cos(\hat{\theta}_i - \hat{\theta}_j), \quad (3.8)$$

where $\hat{V}_i = -i(e_*/C)(\partial/\partial\theta_i)$ is the voltage on the i_{th} grain, and $\langle ij \rangle$ are nearest-neighbor grains in the array. The following is a more common way of writing the Hamiltonian,

$$\hat{H} = \frac{U}{2} \sum_i \hat{n}_i^2 - J \sum_{\langle ij \rangle} \cos(\hat{\theta}_i - \hat{\theta}_j) \quad (3.9)$$

where $U = 4e^2/C$ is the charging energy for a superconducting grain with capacitance C , and the $\hat{n}_i = -i(\partial/\partial\theta_i)$ is the number operator which is conjugate to the phase operator.

In this chapter, we are concerned with a JJA on a square lattice as shown in Fig. 3.2, which shows how the state of the system is dependent on the charging energy U and the Josephson energy J . This figure also illustrates a few important points about the relation between the phase and number operators. When phases are ordered as in Fig. 3.2(a) the system is in a superconducting state and charges are tunneling and moving throughout the lattice. When phases are random as in Fig. 3.2(b), charges are localized on the grain and the system is in an insulating state.

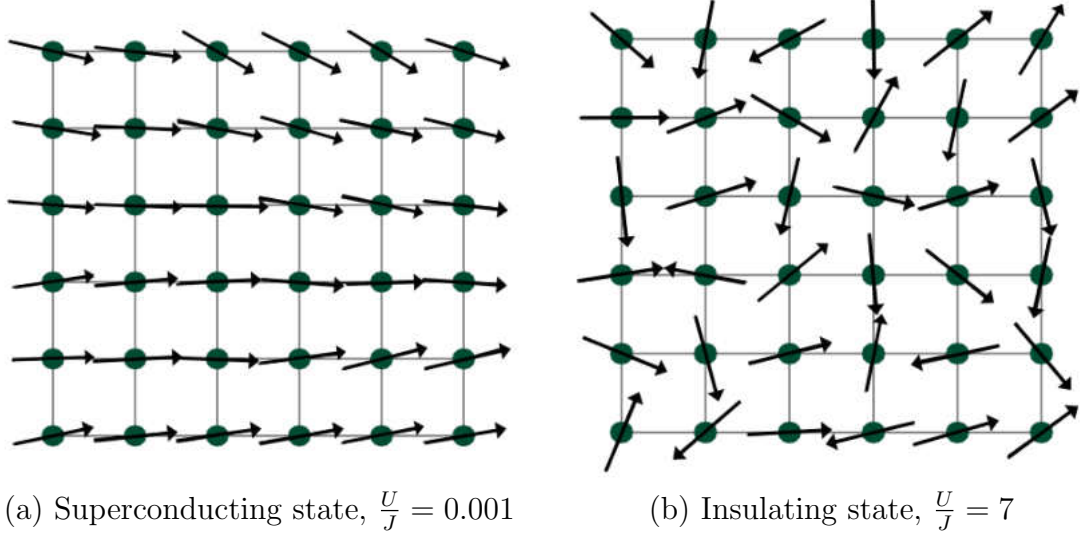


Figure 3.2: Josephson junction array on a square lattice. The black dots represent superconducting grains and the arrows represent phases. (a) When $U \ll J$ the system is in superconducting state, and (b) when $U \gg J$ the system is in insulating state.

This demonstrates that the phase and the charge form a Heisenberg uncertainty pair and the more precisely one knows about one of those variables, the more uncertainty is incurred in the other.

3.3.1 JJA in a perpendicular magnetic field

We now consider a JJA on a square lattice in a perpendicular magnetic field. The Hamiltonian of this “quantum XY model” is

$$\hat{H} = \frac{U}{2} \sum_i \hat{n}_i^2 - J \sum_{\langle ij \rangle} \cos(\hat{\theta}_i - \hat{\theta}_j - A_{ij}). \quad (3.10)$$

A perpendicular magnetic field $\mathbf{B} = B\mathbf{e}_z$ is included via a vector potential in the symmetric gauge $\mathbf{A}(\mathbf{r}) = \frac{1}{2}\mathbf{B} \times \mathbf{r}$ where \mathbf{r} is the position vector. The integrated vector potential A_{ij} from grain i to grain j is

$$A_{ij} = \frac{2e}{\hbar c} \int_{r_i}^{r_j} \mathbf{A}(\mathbf{r}) \cdot d\mathbf{r}.$$

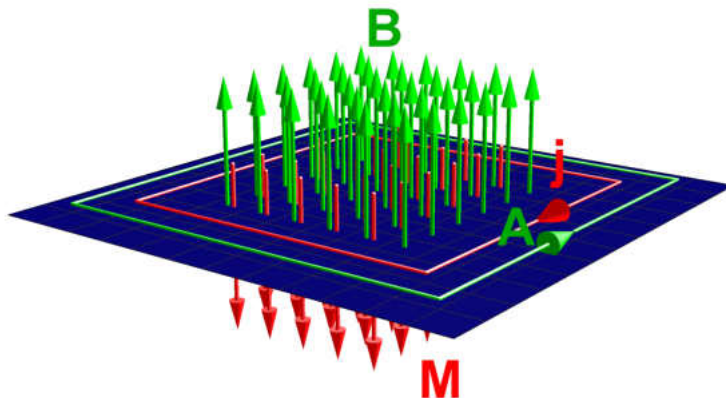


Figure 3.3: Josephson junction array in a perpendicular magnetic field. The direction of the magnetic vector potential A with respect to the magnetic field B is given by the right hand rule. The magnetization M is opposite to the applied B field since a superconductor is diamagnetic in nature, which means that the Meissner screening current j is opposite to A .

Parametrizing the path from i^{th} grain to j^{th} grain as $\mathbf{r} = \mathbf{r}_i + \lambda(\mathbf{r}_j - \mathbf{r}_i)$, where $0 \leq \lambda \leq 1$, gives the following result (derivation in Appendix A3.2),

$$A_{ij} = \frac{2e}{\hbar c} \int_{r_i}^{r_j} \mathbf{A}(\mathbf{r}) \cdot d\mathbf{r} = \frac{2e B_0}{\hbar c} \frac{1}{2} (x_i y_j - x_j y_i).$$

In this chapter we will measure B in the units of $\hbar/2ea^2$. So a magnetic field of strength $B = 2\pi$ corresponds to one flux quantum per plaquette.

3.4 Methods

In the following sections we provide a brief introduction to the Monte Carlo methods used in this study. For a detailed discussion of these methods, a few excellent reviews^{99–101} are suggested.

3.4.1 Variational Monte Carlo (VMC)

Consider a quantum mechanical Hamiltonian

$$\hat{H} = V(\hat{\mathbf{r}}) + \frac{\hat{\mathbf{p}}^2}{2m} \quad (3.11)$$

where $\hat{\mathbf{r}}$ and $\hat{\mathbf{p}}$ are N -component operators satisfying $[\hat{r}_i, \hat{p}_j] = i$ (working in units where $\hbar = 1$). Define a trial wavefunction $\Psi_T(\mathbf{r})$, and let the trial energy be

$$E_T = \frac{\langle \Psi_T | \hat{H} | \Psi_T \rangle}{\langle \Psi_T | \Psi_T \rangle} = \frac{\int d\mathbf{r} |\Psi_T(\mathbf{r})|^2 E_L(\mathbf{r})}{\int d\mathbf{r} |\Psi_T(\mathbf{r})|^2} \quad (3.12)$$

where the *local energy function* $E_L(\mathbf{r})$ is

$$E_L = V - \frac{1}{2m} \frac{\nabla^2 \Psi_T}{\Psi_T} \quad (3.13)$$

where ∇ denotes the gradient with respect to \mathbf{r} . Integrating by parts shows that Eq. (3.12) is also valid with E_L replaced by a *modified local energy function*, which often turns out to be simpler:

$$E_L^{\text{mod}} = V + \frac{1}{2m} \left| \frac{\nabla \Psi_T}{\Psi_T} \right|^2. \quad (3.14)$$

The variational theorem states that E_T is an upper bound to the actual ground state energy E_{gs} . In VMC, one samples configurations from the distribution $|\Psi_T(\mathbf{r})|^2$, and the variational ground state energy is then estimated by averaging the local energy, $E_T = \langle E_L \rangle$.

Generally, $\Psi_T(\mathbf{r})$ is a function of one or more parameters K , so that $E_T(K)$ is also a function of K . Minimizing E_T with respect to K gives a least upper bound to E_{gs} . The accuracy of this method depends on how closely the trial wavefunction $\Psi_T(\mathbf{r})$ approximates the true wavefunction $\Psi_{\text{gs}}(\mathbf{r})$.

In our studies, VMC is not used to estimate observables, but rather, to optimize the trial wavefunction to be used as a guiding wavefunction for diffusion Monte Carlo (DMC).

3.4.2 Diffusion Monte Carlo (DMC)

The wavefunction of the system $\Psi(\mathbf{r}, t)$ obeys the time-dependent Schrödinger equation

$$i\frac{\partial\Psi}{\partial t} = -\frac{1}{2m}\nabla^2\Psi + V\Psi \quad (3.15)$$

(with $\hbar = 1$). Doing a Wick rotation into imaginary time ($t \rightarrow -i\tau$) transforms this into a master equation describing diffusion and decay,

$$\frac{\partial\Psi}{\partial\tau} = \underbrace{D\nabla^2\Psi}_{\text{diffusion}} - \underbrace{V\Psi}_{\text{decay}}, \quad (3.16)$$

with a diffusion constant $D = \frac{1}{2m}$. By expanding $\Psi(\mathbf{r}, \tau)$ in eigenfunctions $\Psi_i(\mathbf{r})$ of the Hamiltonian and taking the spectral decomposition of the time evolution operator, one sees that as $\tau \rightarrow \infty$, $\Psi(\mathbf{r}, \tau)$ evolves toward a multiple of $\Psi_{\text{gs}}(\mathbf{r})$ (the initial wavefunction becomes “projected” onto the ground state wavefunction).

$$|\Psi(\tau)\rangle = e^{-\hat{H}\tau} |\Psi\rangle, \quad (3.17)$$

$$|\Psi(\tau)\rangle = \sum_i e^{-E_i\tau} |\Psi_i\rangle \langle\Psi_i|\Psi\rangle. \quad (3.18)$$

In the long time limit,

$$\lim_{\tau \rightarrow \infty} |\Psi(\tau)\rangle = e^{-E_{\text{gs}}\tau} \langle\Psi_{\text{gs}}|\Psi\rangle |\Psi_{\text{gs}}\rangle \propto |\Psi_{\text{gs}}\rangle.$$

Instead of computing $\Psi(\mathbf{r}, \tau)$ explicitly, one can simulate a set of *walkers* stochastically such that their probability distribution evolves according to Eq. (3.16). This is the

basis of DMC and other projector Monte Carlo methods.

Practical DMC simulations employ importance sampling by introducing a *mixed distribution* $f(\mathbf{r}, \tau) = \Psi_G(\mathbf{r})\Psi(\mathbf{r}, \tau)$, where $\Psi_G(\mathbf{r})$ is a *guiding wavefunction*. With $\Psi = f/\Psi_G$, Eq. (3.16) becomes

$$-\frac{\partial}{\partial \tau} \left(\frac{f(\mathbf{r}, \tau)}{\Psi_G(\mathbf{r})} \right) = -D\nabla^2 \left(\frac{f(\mathbf{r}, \tau)}{\Psi_G(\mathbf{r})} \right) + V(\mathbf{r}) \left(\frac{f(\mathbf{r}, \tau)}{\Psi_G(\mathbf{r})} \right). \quad (3.19)$$

Since the guiding wavefunction is time independent, the above equation can be rewritten as,

$$-\frac{\partial f(\mathbf{r}, \tau)}{\partial \tau} = -D\Psi_G(\mathbf{r})\nabla^2 \left(\frac{f(\mathbf{r}, \tau)}{\Psi_G(\mathbf{r})} \right) + V(\mathbf{r})f(\mathbf{r}, \tau). \quad (3.20)$$

Next, following equality can be shown for the first term in the RHS of Eq. (3.20) shown in appendix A3.1,

$$\Psi_G\nabla^2 \left(\frac{f}{\Psi_G} \right) = \nabla^2 f - 2\nabla \cdot \left(\frac{\nabla\Psi_G}{\Psi_G} f \right) + \left(\frac{\nabla^2\Psi_G}{\Psi_G} \right) f. \quad (3.21)$$

Here the arguments have been dropped for brevity. Plugging the equation (3.21) into (3.20) yields the following equation,

$$\frac{\partial f}{\partial \tau} = D\nabla^2 f - \nabla \cdot \left(2D \frac{\nabla\Psi_G}{\Psi_G} f \right) - D \left(\frac{\nabla^2\Psi_G}{\Psi_G} \right) f - Vf. \quad (3.22)$$

Using the definition of the local energy,

$$E_L = \frac{\hat{H}\Psi_G}{\Psi_G} = -\frac{D\nabla^2\Psi_G}{\Psi_G} + V$$

gives $V = E_L + \frac{D\nabla^2\Psi_G}{\Psi_G}$ which upon replacing into Eq. (3.22) finally gives the following master equation,

$$\frac{\partial f}{\partial \tau} = \underbrace{D\nabla^2 f}_{\text{diffusion}} - \underbrace{\nabla \cdot (\mathbf{v}f)}_{\text{drift}} - \underbrace{E_L f}_{\text{decay}}, \quad (3.23)$$

where $\mathbf{v}(\mathbf{r}) = 2D \frac{\nabla \Psi_G}{\Psi_G}$ plays the role of a *drift velocity* (also known as *quantum force*) and $E_L(\mathbf{r}) = V - \frac{D \nabla^2 \Psi_G}{\Psi_G}$ is a local energy of the same form as Eq. (3.13). Unlike in VMC, in DMC it is *not* acceptable to replace E_L by E_L^{mod} from Eq. (3.14). According to Eq. (3.23), as $\tau \rightarrow \infty$, $f(\mathbf{r}, \tau)$ evolves toward a multiple of the “ground state mixed distribution” $f_{\text{gs}}(\mathbf{r}) = \Psi_G(\mathbf{r}) \Psi_{\text{gs}}(\mathbf{r})$.

From Trotter’s formula, $f(\mathbf{r}, \tau)$ evolves according to

$$f(\mathbf{r}', \tau) = \int d\mathbf{r} G(\mathbf{r}', \mathbf{r}, \tau) f(\mathbf{r}, 0) \quad (3.24)$$

where the Green function is approximately

$$G(\mathbf{r}', \mathbf{r}, \tau) \approx \frac{e^{-\frac{1}{2} \left(\frac{\mathbf{r}' - \mathbf{r} - \mathbf{v}(\mathbf{r})\tau}{\sqrt{2D\tau}} \right)^2}}{\sqrt{2D\tau}} e^{-\frac{E_L(\mathbf{r}) + E_L(\mathbf{r}')}{2} \tau} + \mathcal{O}(\tau^2). \quad (3.25)$$

This is a normal distribution for \mathbf{r}' with mean $\mathbf{r} + \mathbf{v}\tau$ and variance $\sqrt{2D\tau}$, multiplied by a weight function. In the DMC algorithm this corresponds to drift and diffusion of random walkers during a timestep $\delta\tau$,

$$\mathbf{r}' = \mathbf{r} + \underbrace{\mathbf{v} \delta\tau}_{\text{drift}} + \underbrace{\mathbf{X} \sqrt{2D\delta\tau}}_{\text{diffusion}}, \quad (3.26)$$

where \mathbf{X} is a vector of normally distributed independent random numbers, together with a growth/decay process whereby each walker’s weight is multiplied by $\exp \left[-\frac{E_L(\mathbf{r}) + E_L(\mathbf{r}')}{2} \tau \right]$.

3.4.3 Population control

After many timesteps, due to the growth/decay factors, the weights w_n of some walkers will grow to dominate over all others, making the simulation inefficient and inaccurate. To avoid this, one must clone walkers with large weights and delete walkers with small weights (representing birth/death processes), together with some

means of population control to maintain the number of walkers in an acceptable range. For this purpose we adopt the *comb method*. This is a stochastic method for selecting walkers to be discarded or multiplied based on their weights accumulated after the branching process¹⁰², such that the walker population is kept constant. The outline of the method is as follows:

- Find the cumulative weights $C_l = \sum_{n=1}^l w_n$ for $l = 0, 1, 2, \dots, N$, where N is the number of walkers.
- Generate a uniform random variate $\xi \in (0, 1)$.
- For each $k = 1, 2, \dots, M$, where M is the target population, compute $(k-1+\xi)\frac{C_N}{M}$ (the locations of the comb's teeth). (We take $M = N$.)
- Find l such that $C_{l-1} < (k-1+\xi)\frac{C_N}{M} \leq C_l$.

Walker l is selected as many times as the number of teeth that falls between C_{l-1} and C_l , and is discarded if no tooth falls within this range. This is implemented during a resampling step, in which data from walkers to be cloned is used to overwrite data from walkers to be discarded. A similar fixed-population method has yielded accurate results in the simulation of the $S = 1/2$ Heisenberg antiferromagnet using GFMC⁷⁹.

3.4.4 VMC method for Josephson junction array

The JJA Hamiltonian Eq. (3.10) is of the form of Eq. (3.11), with $\hat{\mathbf{r}}_i \rightarrow \hat{\theta}_i$, $\hat{\mathbf{p}}_i \rightarrow n_i$, and $m \rightarrow \frac{1}{U}$. Therefore VMC and DMC methods are applicable.

We only perform VMC calculations at $B = 0$. We use a trial wavefunction of the form

$$\Psi_T(\boldsymbol{\theta}) = \exp \left[\sum_{\langle ij \rangle} K \cos(\theta_i - \theta_j) \right] \quad (3.27)$$

where K is a dimensionless parameter and $\boldsymbol{\theta} = (\theta_1, \theta_2, \dots, \theta_N)$ is the phase configuration. The distribution $|\Psi_T(\boldsymbol{\theta})|^2$ is simply the Boltzmann distribution for a *classical*

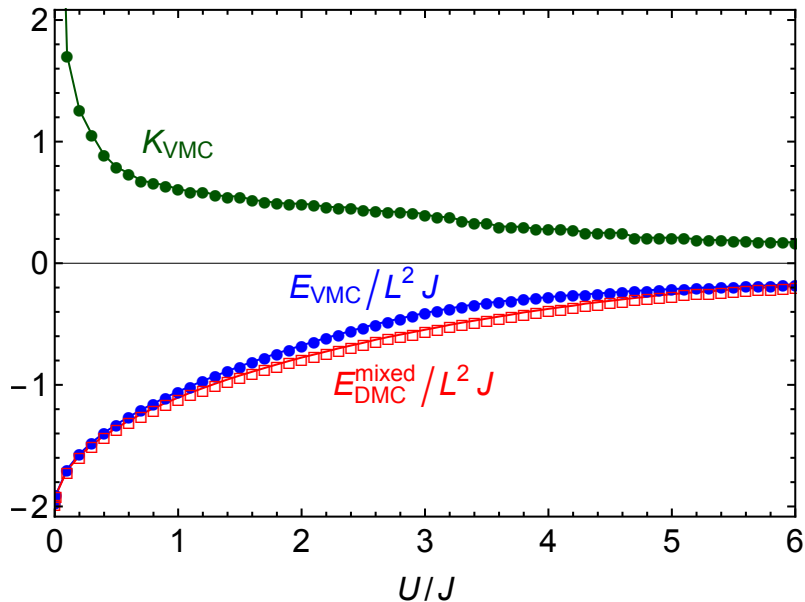


Figure 3.4: Variational Monte Carlo (VMC) results for lattice size $L = 10$ at zero field $B = 0$. The trial energy $E_T(K)$ is minimized with respect to the variational parameter K . The green curve shows the optimal value of K . The blue curve shows E_{VMC} as a function of U/J , which is essentially a least upper bound to the true ground state energy. The red curve shows the DMC ground state energy calculated using the mixed estimator. As expected, $E_{\text{DMC}} \leq E_{\text{VMC}}$. Error bars on energies are too small to display.

XY model at temperature $T = J/2K$, so it can be sampled efficiently using the Wolff algorithm¹⁰³. From Eq. (3.14), the modified local energy function $E_L^{\text{mod}}(\boldsymbol{\theta})$ is

$$E_L^{\text{mod}} = \frac{UK^2}{2} \underbrace{\sum_i \left[\sum_{j@i} \sin(\theta_j - \theta_i) \right]^2}_{f_s(K)} - J \underbrace{\sum_{\langle ij \rangle} \cos(\theta_j - \theta_i)}_{f_c(K)},$$

where j in $j@i$ are all the nearest neighbors of site i . We perform Wolff Monte Carlo simulations at various values of K and tabulate $\langle f_s(K) \rangle$ and $\langle f_c(K) \rangle$. Then, for each value of U/J , we find the optimal variational parameter K_{VMC} that minimizes $\frac{UK^2}{2} \langle f_s(K) \rangle - J \langle f_c(K) \rangle$. See Fig. 3.4.

3.4.5 DMC method for Josephson junction array in perpendicular \mathbf{B} field

For DMC we use the guiding wavefunction

$$\Psi_G(\boldsymbol{\theta}) = \exp \left[\sum_{\langle ij \rangle} K \cos(\theta_i - \theta_j - A_{ij}) \right] \quad (3.28)$$

with $K = K_{\text{VMC}}$. (We find this to be useful even though the VMC simulations are at $B = 0$ whereas the DMC simulations are mostly at $B > 0$.) The diffusion constant is $D = U/2$. The drift velocity $\mathbf{v}(\boldsymbol{\theta})$ is (derivation in Appendix A3.3)

$$v_i = U \frac{\partial_{\theta_i} \Psi}{\Psi} = U \sum_{j @ i} K \sin(\theta_j - \theta_i - A_{ji}).$$

The local energy $E_L(\boldsymbol{\theta}) = \frac{\mathcal{H}\Psi_G}{\Psi_G}$ via similar calculation is,

$$E_L = (UK - J) \sum_{\langle ij \rangle} \cos(\theta_i - \theta_j - A_{ij}) - \frac{UK^2}{2} \sum_j \left[\sum_{i @ j} \sin(\theta_i - \theta_j - A_{ij}) \right]^2.$$

Drift, diffusion, growth/decay, and population control are implemented as described in the previous section. The ground state energy is calculated using the mixed estimator. Other observables (magnetization and vorticity) are calculated using forward walking estimators.

3.5 Calculating observables

3.5.1 Energy

The ground state energy $E_{\text{gs}} = \langle \hat{H} \rangle$ is the easiest observable to calculate in DMC.

From the eigenrelation $\langle \Psi_{\text{gs}} | \hat{H} = \langle \Psi_{\text{gs}} | E_{\text{gs}}$ we find that

$$\frac{\langle \Psi_{\text{gs}} | \hat{H} | \Psi_G \rangle}{\langle \Psi_{\text{gs}} | \Psi_G \rangle} = E_{\text{gs}} = \frac{\int d\mathbf{r} f_{\text{gs}}(\mathbf{r}) E_L(\mathbf{r})}{\int d\mathbf{r} f_{\text{gs}}(\mathbf{r})}. \quad (3.29)$$

Therefore one can obtain an unbiased estimate of the ground state energy using the *mixed estimator* $E_{\text{mixed}} = \frac{1}{N} \sum_{i=1}^N E_L(\mathbf{r}_i)$, which is simply the average local energy of all walkers. A similar result holds for any observable for which the ground state is an eigenstate.

For a general operator diagonal in the configuration basis, $\hat{A} \equiv A(\hat{\mathbf{r}})$,

$$\langle \hat{A} \rangle = \frac{\langle \Psi_{\text{gs}} | \hat{A} | \Psi_{\text{gs}} \rangle}{\langle \Psi_{\text{gs}} | \Psi_{\text{gs}} \rangle} = \frac{\int d\mathbf{r} f_{\text{gs}}(\mathbf{r}) \frac{\Psi_{\text{gs}}(\mathbf{r})}{\Psi_G(\mathbf{r})} A(\mathbf{r})}{\int d\mathbf{r} f_{\text{gs}}(\mathbf{r}) \frac{\Psi_{\text{gs}}(\mathbf{r})}{\Psi_G(\mathbf{r})}}. \quad (3.30)$$

In general, one cannot simply average $A(\mathbf{r}_i)$ over walkers. The extrapolation method¹⁰⁴ is one way to get around this obstacle, but the accuracy of that method depends on the quality of the guiding wavefunction Ψ_G . Instead we use the *forward-walking method*^{105–108}, also known as the *future walking method*. During the simulation, we use cyclic buffers to store ancestry information and configurations for all walkers for the most recent N_{fw} timesteps. After performing step N_{present} , we count $D_i(N_{\text{past}}, N_{\text{present}})$, the number of descendants at step N_{present} that originated from walker i at step $N_{\text{past}} = N_{\text{present}} - N_{\text{fw}}$, and we compute or retrieve $A(\mathbf{r}_i(N_{\text{past}}))$, the value of the observable computed from the configuration of walker i at step N_{past} . This allows us

to construct the *forward walking estimator*

$$A_{\text{FW}} = \frac{\sum_{i=1}^N D_i(N_{\text{past}}, N_{\text{present}}) A(N_{\text{past}}, \mathbf{r}_i)}{\sum_{i=1}^N D_i(N_{\text{past}}, N_{\text{present}})}.$$

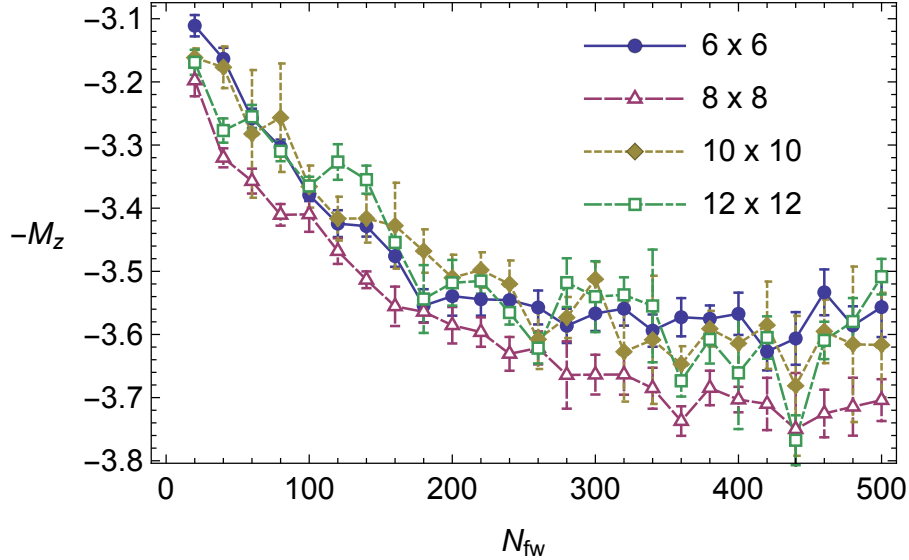


Figure 3.5: Magnetization versus the number of time-steps in the forward walking window N_{fw} . $U = 2$, $B = 0.2$ was used for DMC calculations shown in this plot.

If one uses a large value of N_{fw} , corresponding to a long imaginary time interval $\tau_{\text{fw}} = N_{\text{fw}} \delta\tau$, then it can be shown that $D_i(N_{\text{past}}, N_{\text{present}})$ converges to $\Psi_{\text{gs}}(\mathbf{r}_i)/\Psi_G(\mathbf{r}_i)$. Thus A_{FW} should converge to the true expectation $\langle \hat{A} \rangle$. However, due to the finite population size in DMC, taking N_{fw} too large makes the effective ancestor pool very small, which is also a source of bias. In the results section we investigate the effect of N_{fw} in order to optimize the trade-off between distribution convergence and ancestor pool size.

3.5.2 Magnetization

We define the total magnetization in the lattice as

$$M = \sum_{\langle ij \rangle} \frac{1}{2} (x_i y_j - x_j y_i) I_{ij} \quad (3.31)$$

where I_{ij} is the current flowing from grain i to grain j given by the gauge-invariant expression

$$I_{ij} = \frac{2e}{\hbar c} J_{ij} \sin(\theta_j - \theta_i + A_{ij}). \quad (3.32)$$

We set $2e/\hbar c = 1$ in the simulations.

3.5.3 Vorticity

The vorticity on square $ijkl$ is defined as the gauge-invariant integer Ω_{ijkl} where

$$\Omega_{ijkl} = f_{ij} + f_{jk} + f_{kl} + f_{li}, \quad (3.33)$$

$$f_{ij} = \left\lfloor \frac{\theta_j - \theta_i + A_{ij} + \pi}{2\pi} \right\rfloor, \quad (3.34)$$

where $\lfloor \cdot \rfloor$ represents the floor function. Vorticity obeys a local conservation law: a change of one phase variable, θ_i , changes Ω_{ijkl} values only in the vicinity of grain i , in a way that preserves the total vorticity in the system. We can see this as follows. Every bond ij is associated with an integer f_{ij} . A small change in θ_i or θ_j may cause f_{ij} to change by ± 1 , in which case the vorticities on the adjoining squares change by equal and opposite amounts: if $\Omega_{ijkl} \rightarrow \Omega_{ijkl} \pm 1$, then $\Omega_{jlmn} \rightarrow \Omega_{jlmn} \mp 1$.

Equation (3.33) is similar, but not quite the same, as the definition of vorticity in Ref. 109. For a particular phase configuration, Ω_{ijkl} is an integer on every plaquette; however, the quantum mechanical average vorticity $\langle \Omega_{ijkl} \rangle$ is generally not an integer.

3.6 Results

VMC calculations were done on $L = 10$ lattices with periodic boundary conditions, for 72 values of K and at zero field $B = 0$. Each simulation was run for 400000 steps (Wolff updates). Figure 3.4 shows the ground state energy upper bound E_{VMC} and optimal trial wavefunction parameter K_{VMC} as functions of U/J . As described earlier, the optimized VMC trial wavefunction is used as the guiding wavefunction in DMC.

DMC simulations were done on lattices with $L = 6, 8, 10, 12$ with Neumann boundary conditions (BCs), at four different magnetic field values $B = 0.1, 0.2, 0.3, 0.4$. Neumann BCs are physically more realistic than periodic BCs and allows us to apply arbitrary B fields unrestricted by lattice sizes. The first 1000–5000 time steps were used for “equilibration” allowing the estimators to converge to their actual values, and the data was collected for 9000–12000 time steps. Bigger lattices in higher magnetic fields required more time steps for equilibration and data collection. All simulations were performed with 1000 walkers. (We verified that increasing the population size beyond 1000 did not significantly alter the results.) Since the typical distance diffused in one step is $\sqrt{U\tau}$, for increasing values of U/J the timestep was gradually decreased from $\tau = 0.2$ to $\tau = 0.005$.

We chose the number of time-steps in the forward walking window in the range $N_{\text{fw}} = 200\text{--}300$. Figure 3.5 shows that the estimator values are reasonably converged when $N_{\text{fw}} > 200$ for all three lattice sizes.

Errors in the estimators were calculated using the on-the-fly binary reblocking method¹¹⁰.

Figures 3.6, 3.7, 3.8, and 3.9 show the energy and magnetization graphs for $B = 0.1, 0.2, 0.3, 0.4$ respectively. Both quantities were calculated both with and without a guiding wavefunction. The magnetization is affected more severely by the absence

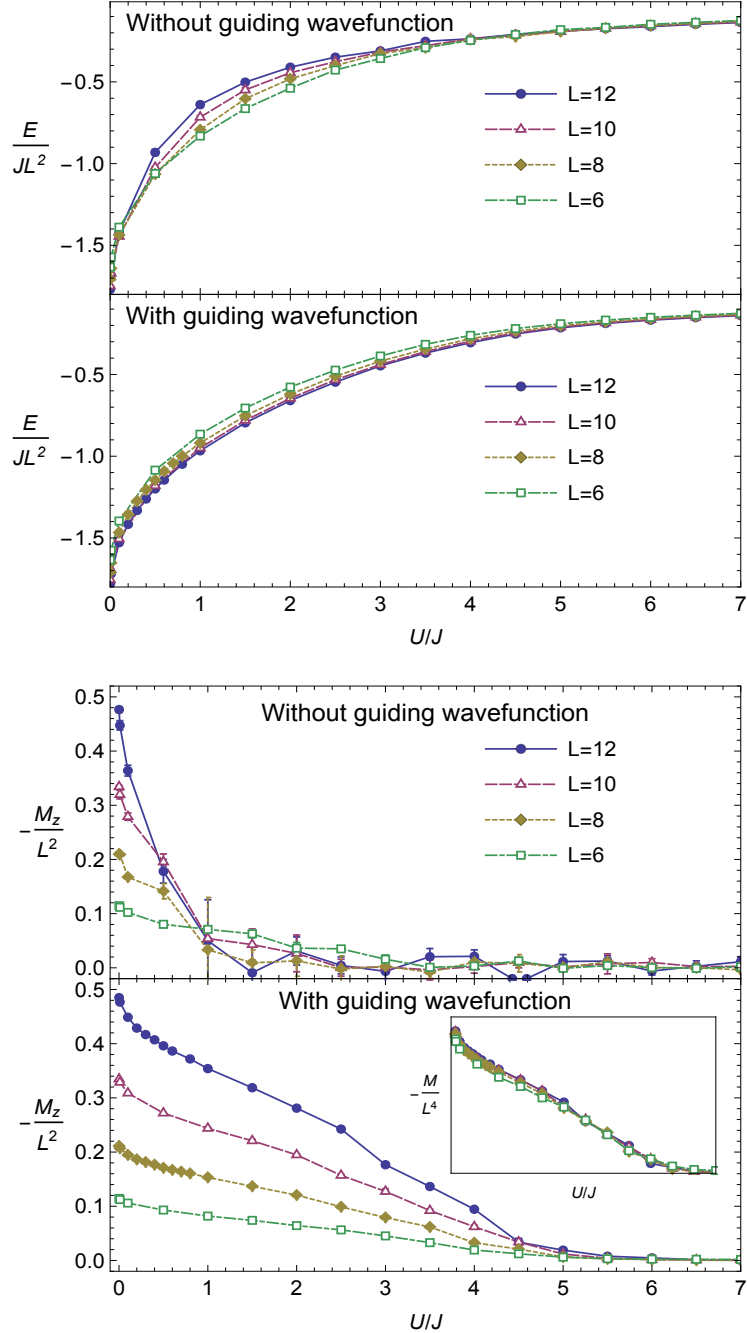


Figure 3.6: Energy (top) and magnetization (bottom) versus U/J for lattices $L = 6, 8, 10, 12$ for magnetic field $B = 0.1$, from DMC calculations with (bottom) and without (top) a guiding wavefunction. The magnetization has large error bars without a guiding wavefunction indicating that it is necessary to obtain accurate results for quantities other than energy. The inset shows the $M \sim L^4$ scaling of the magnetization in absence of an intermediate vortex state.

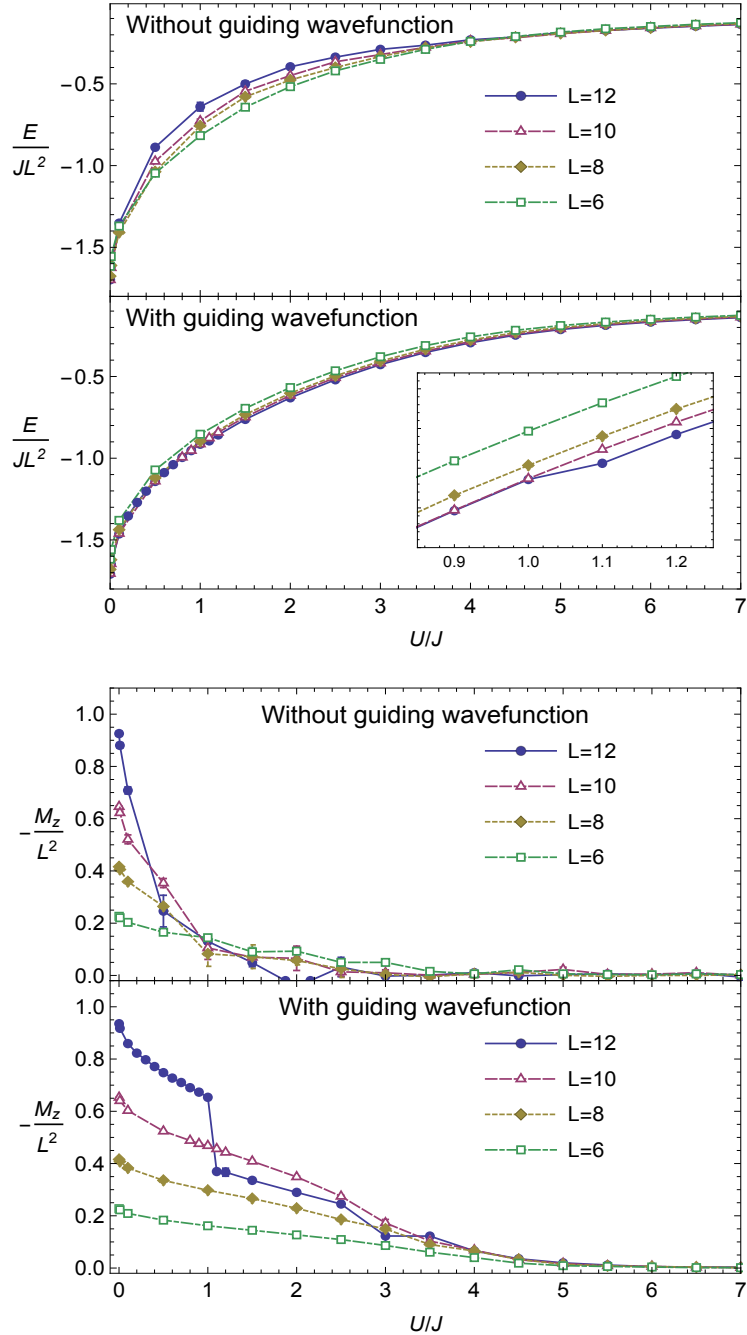


Figure 3.7: Energy (top) and magnetization (bottom) versus U/J for lattices $L = 6, 8, 10, 12$ for magnetic field $B = 0.2$. The inset shows a kink in the energy corresponding to a big drop in the magnetization caused by vortex entry as can be seen in Fig. 3.10.

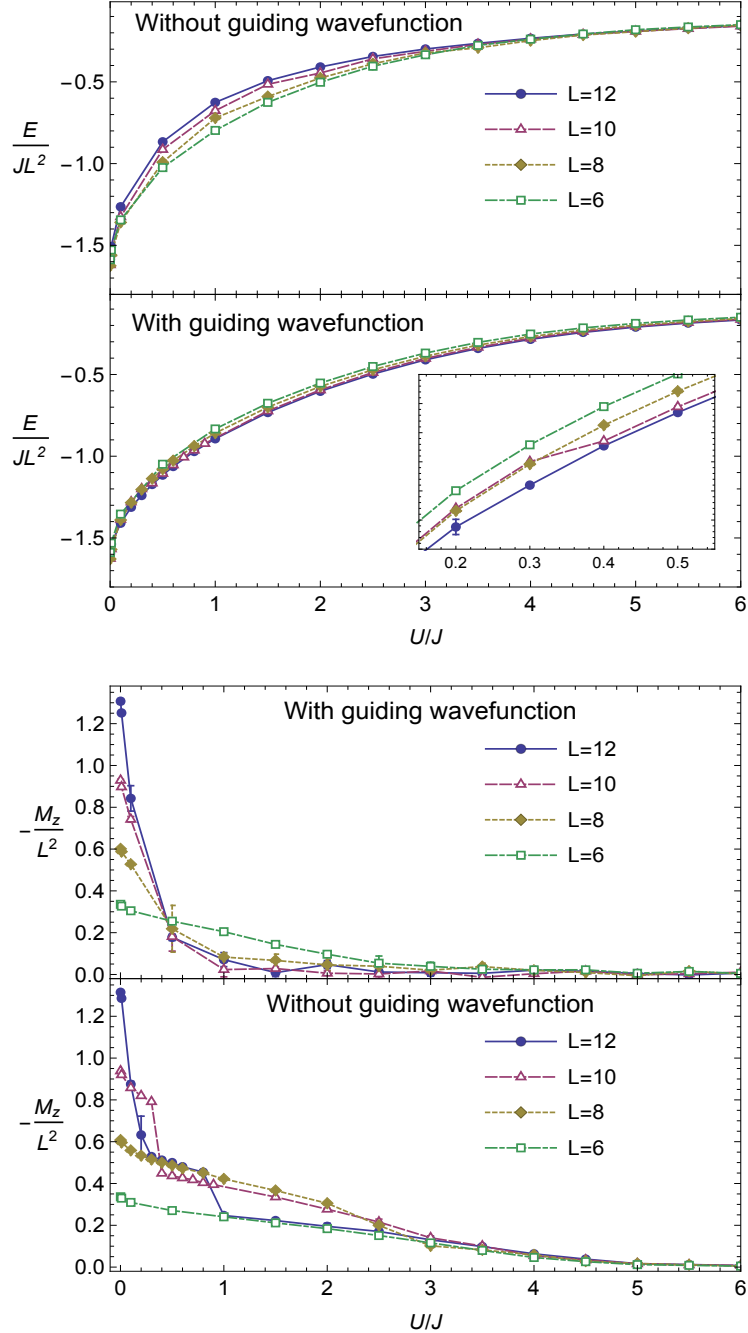


Figure 3.8: Energy (top) and magnetization (bottom) versus U/J for lattices $L = 6, 8, 10, 12$ for magnetic field $B = 0.3$. Magnetization drop can be seen for $L = 10$ and $L = 12$ lattice around $U/J \approx 0.4$ and $U/J \approx 1$. The inset shows a kink in the energy only for $L = 10$ due to lack of space, but every magnetization drop is accompanied by a kink in the energy. Again, the drops in magnetization can be traced to a vortex entry shown in Fig. 3.10.

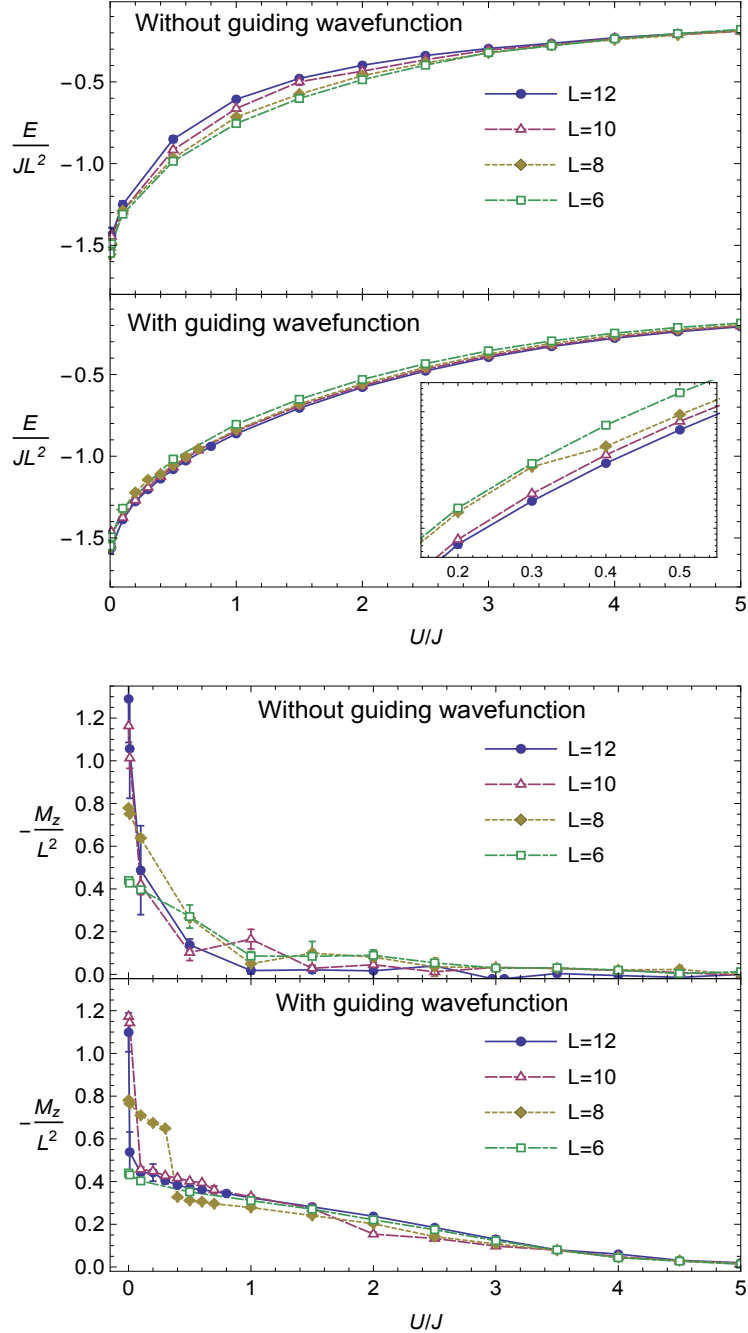


Figure 3.9: Energy (top) and magnetization (bottom) versus U/J for lattices $L = 6, 8, 10, 12$ for magnetic field $B = 0.4$. Magnetization drop can be seen for $L = 8$, $L = 10$ and $L = 12$ lattice around $U/J \approx 0.1$, $U/J \approx 0.4$ and $U/J \approx 1$. Vortex entry for these values is shown in Fig. 3.10. The magnetization scales as $M \sim L^2$ during the vortex melting.

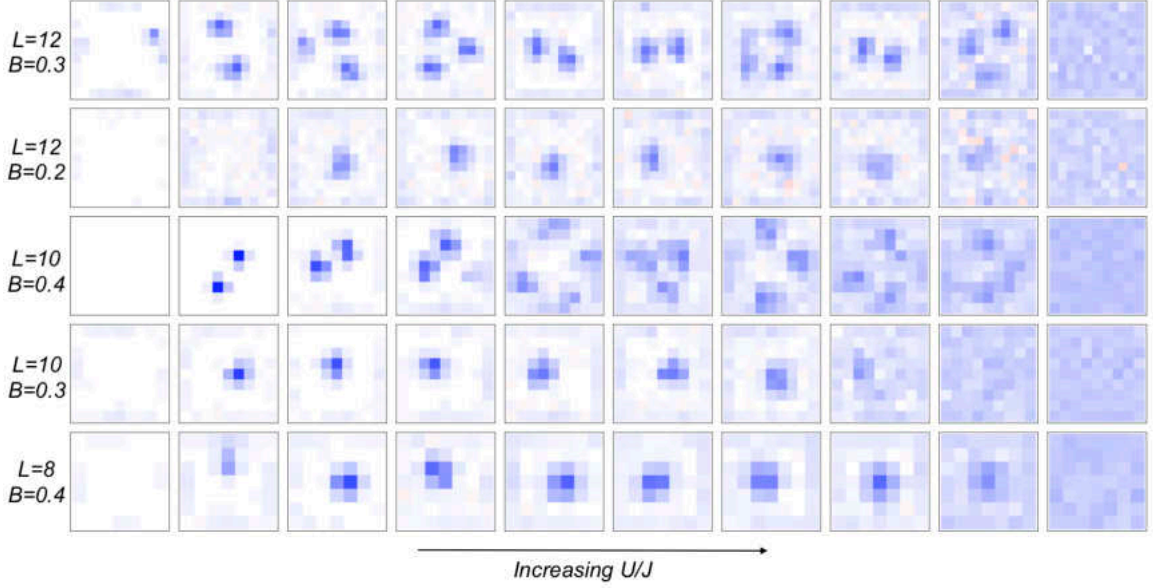


Figure 3.10: Vorticity plots for lattice sizes L and magnetic fields B . Vortex formation is seen to occur mostly around $U/J \approx 0.4$ and $U/J \approx 1$ which causes abrupt drop in the magnetization and a kink in the energy. Further increasing U/J causes vortex melting. Following are U/J values going from left to right ordered in rows from top to bottom:

1st row: $U/J = 0.2, 0.5, 0.6, 0.7, 0.8, 0.9, 1, 1.1, 2, 4.5$.

2nd row: $U/J = 0.3, 1, 1.1, 1.2, 1.3, 1.4, 1.5, 1.7, 2.5, 5$.

3rd row: $U/J = 0.01, 0.1, 0.3, 0.5, 0.7, 0.9, 1, 1.5, 2, 5$.

4th row: $U/J = 0.3, 0.4, 0.5, 0.6, 0.7, 0.8, 0.9, 1.5, 3, 8.5$.

5th row: $U/J = 0.2, 0.4, 0.5, 0.6, 0.7, 0.8, 0.9, 1, 2, 3$.

of guiding wavefunction as seen in figures 3.6-3.9. The magnetization M_z is in the opposite direction of the applied B field because the system is diamagnetic in the superconducting state. In the insulating state the magnetization is zero as expected. Abrupt drops in the magnetization curves for $L = 8, 10, 12$ lattices are due to vortices entering the system from the edges. Corresponding to such a drop is a kink in the energy graph, albeit a small one which can be seen in insets within the energy graphs. Figure 3.9 shows the magnetization drops for $B = 0.4$ in $L = 12$ lattice occurring at $U/J \approx 0.01$, for $L = 10$ occurring at $U/J \approx 0.1$, and for $L = 8$ occurring at $U/J \approx 0.4$. Figure 3.8 shows the magnetization drops for $B = 0.3$ in $L = 12$ lattice occurring at $U/J \approx 0.4$ and $U/J \approx 1$, and for $L = 10$ occurring at $U/J \approx 0.4$.

Figure 3.7 shows the magnetization drop for $B = 0.2$ in $L = 12$ lattice occurring at $U/J \approx 1$. Figure 3.10 shows the spatial dependence of vorticity for $L = 8, 10, 12$ where vortices can be seen for U/J values corresponding to the abrupt drops in the magnetization and kink in the energy.

3.7 Discussion and conclusions

Abrupt drops in magnetization and kinks in energy curves are caused by vortex formation. Increasing U/J causes “melting” in analogy to thermal melting of vortex lattices in the experiments of Ling et al¹¹¹. The vorticity field is a natural indicator of quantum melting in the simulations. For $B = 0.1$, the magnetization scales as $M \sim L^4$ all the way to the SIT, as expected for a superconducting film exhibiting the Meissner effect. For $B = 0.4$ the magnetization drops due to vortex formation, changing the scaling to $M \sim L^2$ during the vortex melting. Between $B = 0.1$ and $B = 0.4$ scaling is not clear, and to shed more light into the nature of this intermediate vortex state we plan to simulate larger systems by parallelizing the DMC algorithm.

We have applied DMC to a lattice model for the first time and our results show that DMC is a viable method for simulating lattice models. Below, we outline a comparison between DMC and PIMC (one of the most commonly used Monte Carlo methods for simulating JJAs).

- DMC is inherently a zero-temperature method whereas PIMC is a finite-temperature method. PIMC results must be extrapolated to zero temperature, but this may require making unjustified assumptions about critical exponents¹¹².
- The ground state energy $E_{\text{gs}} = \langle \hat{H} \rangle$ can be calculated simply and accurately in DMC. In PIMC, because \hat{H} contains both the position operator $\hat{\mathbf{r}}$ and momentum operator $\hat{\mathbf{p}}$, naïve energy estimators fail and one has to resort to

complicated techniques such as virial estimators¹¹³.

- In DMC, calculating quantities whose operators do not commute with \hat{H} requires the forward walking algorithm, whereas calculating any quantity that contains only $\hat{\mathbf{r}}$ is straightforward in PIMC.
- DMC only gives equal-time correlations, which prevents us from using Kubo formulas to calculate static response functions such as superfluid stiffness and diamagnetic susceptibility. These quantities can be calculated in PIMC.
- Computer memory storage requirement in DMC is $L_x \times L_y \times N_w$ where L_x and L_y are lattice dimensions and N_w is the number of walkers (1000 in this work); In PIMC it is $L_x \times L_y \times N_\tau$, where N_τ is the number of time slices in imaginary time. Many authors like to use $N_\tau = L_x = L_y$ ^{82,114}. However, careful PIMC studies by ourselves (unpublished) suggest that imaginary time discretization error ($\delta\tau$ error) in PIMC can be very large for the values that are currently being used for N_τ , leading to the critical value of U/J being off by a factor of 3. It is necessary to go to $N_\tau > 2000$ in order to get accurate critical values.
- Both DMC and PIMC are subject to Monte Carlo statistical errors, which scale as $1/\sqrt{N_{steps}}$ where N_{steps} is the number of Monte Carlo steps. In addition, systematic bias in DMC is due to population control bias¹¹⁵ and time-step error incurred due to Trotter decomposition, whereas systematic bias in PIMC is due to $\delta\tau$ error.
- DMC is more favorable to parallel computing¹¹⁶. Parallelization can be done on a supercomputing cluster or a CUDA programming language enabled graphics processing unit. We plan to pursue the latter route in order to simulate larger lattices.

The DMC method is a useful check against the PIMC method due to the com-

plementary behavior of errors and scaling. Within the DMC itself, the guiding wavefunction is crucial for accurately estimating quantities whose operators do not commute with the Hamiltonian. Using the guiding wavefunction also helps to achieve a lower ground state energy in the region where the on-site Coulomb interactions and the nearest-neighbor Josephson couplings are competitive. The forward walking algorithm produced excellent results in this study as expected from the past studies^{106,108}. After all the considerations, we conclude that the DMC with an importance sampling is a natural and appropriate choice, complementary to PIMC, for simulating lattice models at zero temperature.

In the future, we plan to parallelize the DMC algorithm to simulate a JJA in a larger lattice or a multi-condensate JJA in search for more interesting physics.

CHAPTER IV

2D ANISOTROPIC ISING MODEL IN UNIAXIALLY STRAINED $\text{Hf}_2\text{MnC}_2\text{O}_2$

This chapter describes Monte Carlo simulations of Ising models applied to the prediction of ferromagnetic critical temperature in the 2D material of $\text{Hf}_2\text{MnC}_2\text{O}_2$.

4.1 Ising model

The Hamiltonian of an Ising model can be written as,

$$H = -J \sum_{\langle ij \rangle} \sigma_i \sigma_j - h \sum_i \sigma_i, \quad (4.1)$$

where $\sigma_i = \pm 1$ are Ising spins, $\langle ij \rangle$ indicates that the sum is over nearest neighbors, h is the external magnetic field, and J is the strength of interaction between the spins. Exact solutions of this model exists only in 1D (for zero and non-zero h) and in 2D in the absence of an external magnetic field (when $h = 0$). Following is the summary of the two important analytical approaches.

4.2 Historically important analytical solutions of 2D Ising model

4.2.1 Onsager's solution

In Onsager's 1944 paper³¹ he solved the anisotropic Ising model on a square lattice in the thermodynamic limit ($N \rightarrow \infty$) for the case $h = 0$. The anisotropic Ising model has different interaction strengths, J_1 and J_2 , in x and y directions, which modifies Eq. (4.1) to

$$H = -J_1 \sum_{\langle ij \rangle_x} \sigma_i \sigma_j - J_2 \sum_{\langle ij \rangle_y} \sigma_i \sigma_j. \quad (4.2)$$

For the above model, he obtained the following expression for the free energy F ,

$$\begin{aligned} \beta F = & -\ln 2 \\ & - \frac{1}{8\pi^2} \int_0^{2\pi} d\theta_1 \int_0^{2\pi} d\theta_2 \ln[\cosh 2\beta J_1 \cosh 2\beta J_2 - \sinh 2\beta J_1 \cos \theta_1 - \sinh 2\beta J_2 \cos \theta_2]. \end{aligned} \quad (4.3)$$

He used the transfer matrix method in which the operators in this problem were expanded "as linear combinations of the generating basis elements of an algebra which can be decomposed into direct products of quaternion algebras"³¹. He also claimed the following expression for the spontaneous magnetization without a detailed proof:

$$M = (1 - \Omega^{-2})^{\frac{1}{8}} \quad \text{where} \quad \Omega = \sinh\left(\frac{2J_1}{k_B T}\right) \sinh\left(\frac{2J_2}{k_B T}\right). \quad (4.4)$$

In 1952, Chen Ning Yang was able to derive the expression for the spontaneous magnetization¹¹⁷, not without much difficulty as he recalled years later that this derivation was the longest calculation of his career.

4.2.2 Kac and Ward's approach

In 1952³⁵, Kac and Ward re-derived Onsager's result using a simpler approach based on a combinatorial technique, which became the basis for many other methods. The idea behind this approach was to expand sums in the exponential into products of exponentials in the partition function,

$$Z = \sum_{\{s_i\}} e^{\beta J \sum_{\langle ij \rangle} \sigma_i \sigma_j} = \sum_{\{s_i\}} \prod_{\langle ij \rangle} e^{\beta J \sigma_i \sigma_j}. \quad (4.5)$$

Since the product $\sigma_i \sigma_j = \pm 1$, the exponential term simplifies to:

$$e^{\beta J \sigma_i \sigma_j} = \cosh \beta J (1 + \tanh(\beta J) \sigma_i \sigma_j). \quad (4.6)$$

The partition function can then be written as,

$$Z = (\cosh \beta J)^N \sum_{\{s_i\}} \prod_{\langle ij \rangle} (1 + \tanh(\beta J) \sigma_i \sigma_j). \quad (4.7)$$

Kac and Ward calculated $\prod_{\langle ij \rangle} (1 + \tanh(\beta J) \sigma_i \sigma_j)$ using a combinatorial approach of summing over all polygons that can be drawn on the square lattice. After deriving the partition function, other quantities of interest can then be calculated using it.

Kasteleyn found yet another combinatorial solution to the Ising model by mapping it into a “dimer problem” which makes use of Pfaffian, which is related to finding the determinant of a skew-symmetric matrix³². These combinatorial methods are considered to be easier to understand.

4.3 Computational method

Another approach to solving the Ising model is a computational method based on the Monte Carlo method. We used a Monte Carlo method with the Wolff single-cluster

algorithm¹¹⁸ because it can be easily generalized to multilayers or 3D if necessary for future work.

4.3.1 Wolff single-cluster algorithm

The first effective algorithm used in a Monte Carlo method was the Metropolis algorithm^{119,120} in which spins are flipped one at a time. However, this algorithm suffers from critical slowing, meaning that near the critical temperature T_c the simulation takes a very long time to explore the typical set of configurations. Cluster algorithms were developed to circumvent the critical slowing down by flipping cluster of spins rather individual spins. Swendsen-Wang¹²¹ and Wolff single-cluster algorithms¹⁰³ are the commonly used cluster algorithms. In this study, we used the Wolff single-cluster algorithm because it is faster of the two. Monte Carlo simulations must satisfy two important conditions; detailed balance, and ergodicity.

4.3.2 Detailed balance

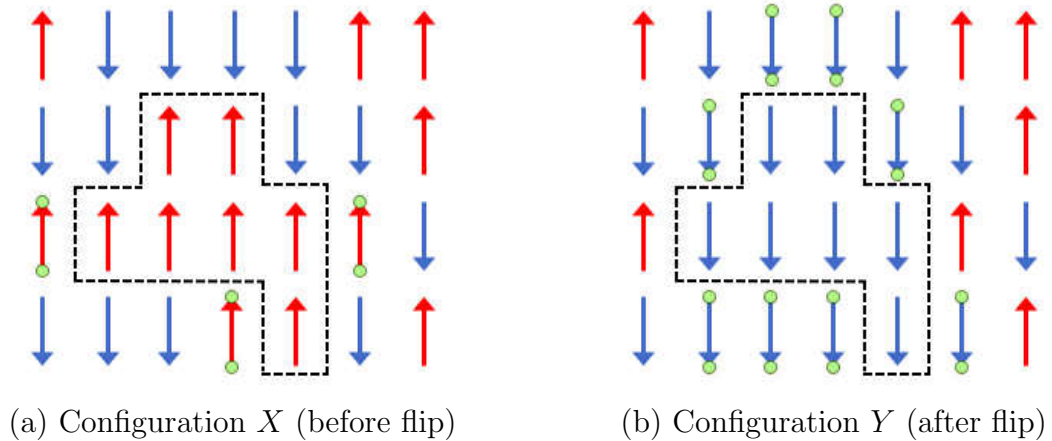


Figure 4.1: Configurations before and after a flip of a cluster (marked by the dotted lines). Red arrows represent spin up and blue arrows represent spin down. Spins immediately outside the cluster with similar orientation as the spins inside the cluster are marked with a green circle at the base and head of the arrows.

Figure 4.1 shows two different configurations, X and Y . Suppose we started with configuration X and picked any one random site. Then the four neighboring spins from the spin in that site are added with some probability P_{add} . If a spin is accepted then it is added to the cluster. The same procedure is then applied to the neighbors of this new spin. This process is carried out throughout the lattice iteratively. In the case of configuration X , the cluster has grown to include 7 spins. This cluster can then be flipped to achieve configuration Y . Now imagine, going in the reverse direction, i.e. from configuration Y to X . The probability of choosing the seed site is the same, and the probability of adding spins to the cluster is the same as well. The only difference is the energy cost for breaking the bonds of like spins that were not added to the cluster. For example, in configuration X there are 3 red (up) spins sharing a bond with the red spins inside the cluster whereas in configuration Y there are 8 such blue (down) spins. The probability of not adding any single spin is $1 - P_{\text{add}}$, which is proportional to the selection probability $P(X \rightarrow Y)$. The probability for not adding 3 spins is $(1 - P_{\text{add}})^3$ (in case of configuration X), and that for 8 spins is $(1 - P_{\text{add}})^8$ (in the case of configuration Y). Generalizing to m and n number of such spins that are not added to the cluster for configurations X and Y respectively, the condition for detailed balance is given by,

$$\frac{P(X \rightarrow Y) A(X \rightarrow Y)}{P(Y \rightarrow X) A(Y \rightarrow X)} = (1 - P_{\text{add}})^{m-n} \frac{A(X \rightarrow Y)}{A(Y \rightarrow X)} = e^{-\beta(E_X - E_Y)}. \quad (4.8)$$

In equation Eq. (4.8), $A(X \rightarrow Y)$ and $A(Y \rightarrow X)$ represent the acceptance ratios for going from one configuration to another. Since there are m broken bonds for going from configuration $X \rightarrow Y$, the change in energy of the system is $+2Jm$, where J is the interaction energy between the neighboring bond. For the n bonds created in the configuration Y the energy changes by $-2Jn$. Therefore the total energy difference

is,

$$E_X - E_Y = 2J(m - n). \quad (4.9)$$

Then, equation Eq. (4.8) can be rewritten as,

$$\frac{A(X \rightarrow Y)}{A(Y \rightarrow X)} = (e^{2\beta J}(1 - P_{\text{add}}))^{n-m}, \quad (4.10)$$

which leads to a very convenient option. If the probability P_{add} of adding a spin into the cluster is chosen to be,

$$P_{\text{add}} = 1 - e^{2\beta J}, \quad (4.11)$$

the right hand side term of Eq. (4.10) becomes 1, making $A(X \rightarrow Y) = A(Y \rightarrow X)$. This means that the acceptance ratios for going forward or backward is always equal 1, due to which flipping of the cluster is never rejected. In this way, not only does the Wolff single-cluster algorithm satisfy the detailed balance condition, but every proposed move is accepted. The above analysis applies to the Ising model with two interaction energies J_1 and J_2 as well.

4.3.3 Ergodicity

Ergodicity is the ability of an algorithm to effectively explore all of the configuration space of the system. For an algorithm to be ergodic the algorithm must be able to go from any one configuration to any other configuration in a finite number of time-steps. In the case of the Wolff cluster algorithm, ergodicity is satisfied because single spin flips are possible as well, so the simulation can explore all configurations.

4.3.4 Summary of Wolff algorithm

Together, detailed balance and ergodicity are necessary and sufficient conditions for the system to evolve to equilibrium. The time it takes for a system to approximately

reach the equilibrium is called the equilibration time, and the data collection process is started only after this period.

In short, the Wolff algorithm can be summarized as follows:

- Select a spin from a random site.
- Add the nearest neighbors of this spin to the cluster with a probability $P = 1 - e^{-2\beta J}$.
- If a new spin is added to the cluster, consider adding the nearest neighbors of this spin to the cluster in the same way as in step 2.
- Repeat steps 2 and 3 until the same process is iterated throughout the lattice.
- Flip the final cluster.

4.4 Hf₂MnC₂O₂ MXene

In this chapter, the 2D anisotropic Ising model is used to calculate the Curie temperature T_c for a monolayer Hf₂MnC₂O₂ MXene under uniaxial strain. MXenes are 2D materials that are transition metal carbides or nitrides. Fig. 4.2 shows the MXene of interest from top and side view. The strain is applied in either the armchair direction (y) or the zig-zag direction (x). In the Hf₂MnC₂O₂ monolayer, only the Mn atoms contribute to magnetic properties of the system according to the density functional theory (DFT) simulations. The DFT simulations were performed by another group from our department, so the details of those calculations are not within the scope of this chapter. Beyond certain strain values (9% in the armchair and 7% in zig-zag) this MXene monolayer becomes a half-metal, where only electrons whose spins are oriented in a particular direction crosses the Fermi level making them available for spintronic applications. This system shows increasing T_c for increasing strain.

The Mn atoms are arranged in a triangular lattice. We approximated the magnetic behavior of $\text{Hf}_2\text{MnC}_2\text{O}_2$ by a classical spin-half Ising model on a triangular lattice, with strain-induced anisotropy. The Hamiltonian is¹²²

$$H = E_0 - J_1 \sum_{\langle ij \rangle_x} \sigma_i \sigma_j - J_2 \sum_{\langle ij \rangle_{\text{diag}}} \sigma_i \sigma_j, \quad (4.12)$$

where $\sigma_i = \pm 1$ are Ising spins, $\langle ij \rangle_x$ indicates that the sum is over nearest neighbors in the horizontal (x) direction, $\langle ij \rangle_{\text{diag}}$ indicates nearest neighbors in other directions, J_1 and J_2 are couplings along horizontal and diagonal directions as shown in Fig. 4.3, and E_0 represents the non-magnetic part of the energy.

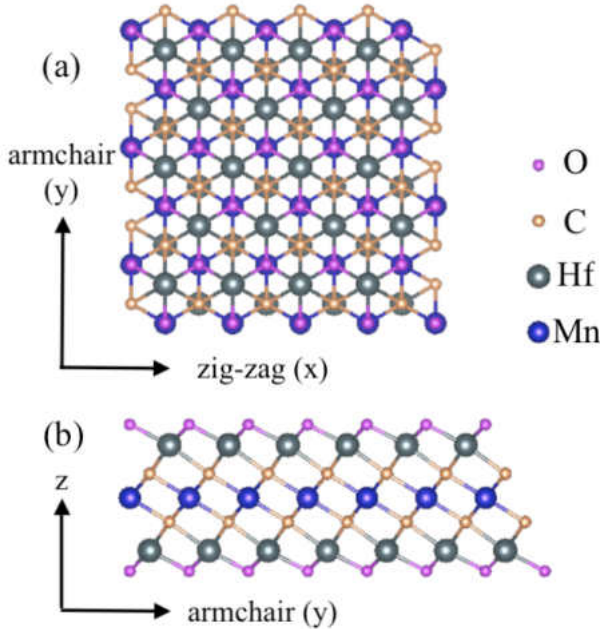


Figure 4.2: (a) Top and (b) side views of the $\text{Hf}_2\text{MnC}_2\text{O}_2$ monolayer with the height in z direction, and remaining two directions (x and y) in which strain is applied uniaxially.

In order to find the magnetic ground state of the monolayer at each value of applied strain, the total energies for various ferromagnetic (FM), antiferromagnetic (AFM), and non-magnetic (NM) configurations as illustrated in Fig. 4.3 were calculated using DFT. In the AFM1 configuration [Fig. 4.3(b)], spin-down Mn atoms form straight lines, whereas in AFM2 [Fig. 4.3(c)] they form zig-zag lines. AFM3 [Fig. 4.3(d)] has spin-down stripes that are two sites

thick. AFM4 [Fig. 4.3(e)] is the same as AFM1 rotated by 120° . E_{FM} has the lowest energy compared to any of the other configurations. Thus the ground state is ferromagnetic under uniaxial strain within the range -4% to 10% . $E_{\text{NM}} - E_{\text{FM}}$ is higher

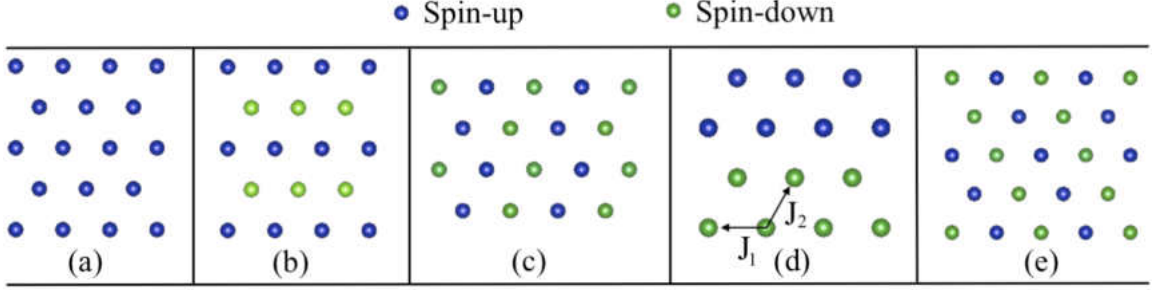


Figure 4.3: (a) FM, (b) AFM1, (c) AFM2, (d) AFM3 and (e) AFM4 spin configurations with coupling J_1 and J_2 in two different directions. Only Mn atoms are considered, since contribution for magnetic moment from other atoms are negligible.

than 2.3 eV whereas $E_{\text{AFM}} - E_{\text{FM}}$ is always very low (less than 0.2 eV).

According to Eq. 4.12, the energies of the spin configurations in Fig. 4.3(a,b,e) are

$$E_{\text{FM}} = E_0 - J_1 - 2J_2 \quad (4.13)$$

$$E_{\text{AFM1}} = E_0 - J_1 + 2J_2 \quad (4.14)$$

$$E_{\text{AFM4}} = E_0 + J_1. \quad (4.15)$$

Solving for the couplings yields $J_1 = \frac{1}{4}(2E_{\text{AFM4}} - E_{\text{AFM1}} - E_{\text{FM}})$ and $J_2 = \frac{1}{4}(E_{\text{AFM1}} - E_{\text{FM}})$, which allows us to infer J_1 and J_2 from the results of DFT energy calculations. Thus, we obtain J_1 and J_2 as a function of uniaxial strain ε_x or ε_y .

4.5 Calculated quantities

Graphs for the calculated quantities are similar for strain in both the zig-zag and arm-chair direction. So only graphs for strain in the zig-zag direction are shown.

4.5.1 Energy

Calculating energy is straightforward in the Ising model simulation. It follows simply from the Hamiltonian. The Monte Carlo estimator for the energy is obtained using,

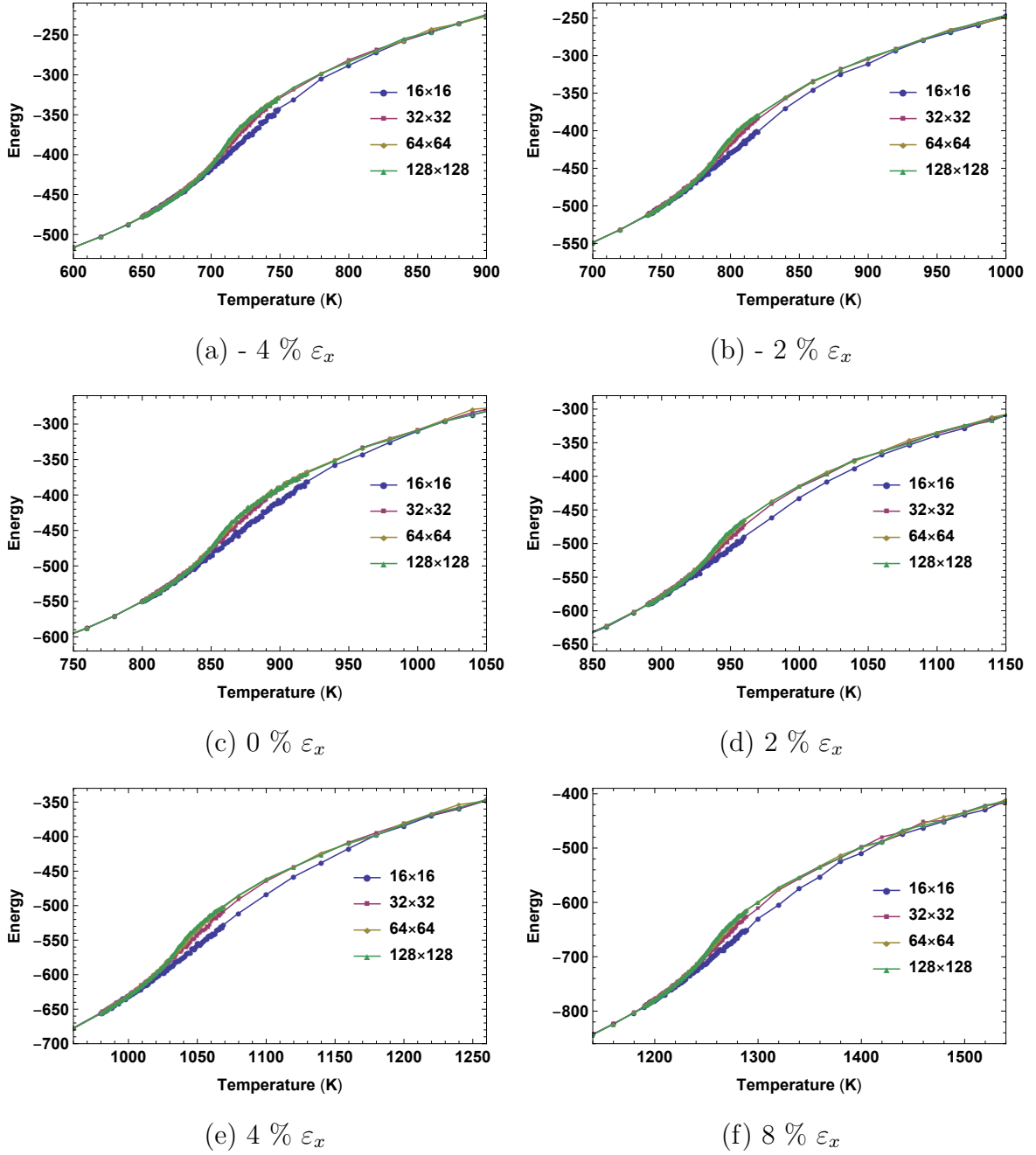


Figure 4.4: Energy vs. temperature for different strain values in the x direction. There is an inflection point around the Curie temperature which would correspond to a divergence in the specific heat curve in the thermodynamic limit.

$$\langle E \rangle = \frac{1}{N} \left(-J_1 \sum_{\langle ij \rangle_x} \sigma_i \sigma_j - J_2 \sum_{\langle ij \rangle_{\text{diag}}} \sigma_i \sigma_j \right), \quad (4.16)$$

where N is the total number of Monte Carlo steps after equilibration. In our implementation, the energy is calculated for individual spins interacting with their nearest neighbors in both x and $diag$ directions at each time-step. Since this process is done iteratively for all surrounding spins every interaction is double counted, so the sum must be divided by two to obtain the correct value for the total energy. Results are shown in Figure 4.4, for different strain values in the zig-zag direction. The inflection point occurs at the critical point T_c (corresponding to this inflection point is an abrupt jump in the specific heat $c_V(T)$ graph), which is also called the Curie temperature in ferromagnetic systems.

4.5.2 Heat capacity

Heat capacity can be calculated by taking the derivative of energy with respect to the temperature. Numerical differentiation is prone to error. Thus, the fluctuation-dissipation theorem becomes useful in this case. The following derivation gives a direct estimator for the heat capacity:

$$C_V = \frac{\partial \langle E \rangle}{\partial T} \quad (4.17)$$

$$= -\frac{\beta}{T} \frac{\partial \langle E \rangle}{\partial \beta} \\ = \frac{\beta}{T} \frac{\partial^2 \ln Z}{\partial \beta^2} \quad (4.18)$$

$$= \frac{\beta}{T} \frac{\partial}{\partial \beta} \left(\frac{1}{Z} \frac{\partial Z}{\partial \beta} \right) = \frac{\beta}{T} \left[\frac{1}{Z} \frac{\partial^2 Z}{\partial \beta^2} - \left(\frac{1}{Z} \frac{\partial Z}{\partial \beta} \right)^2 \right], \quad (4.19)$$

and finally,

$$C_V = \frac{\beta}{T} [\langle E^2 \rangle - \langle E \rangle^2]. \quad (4.20)$$

The following identities and definition were used in the derivation,

$$\langle E \rangle = -\frac{1}{Z} \frac{\partial Z}{\partial \beta}, \quad \langle E^2 \rangle = -\frac{1}{Z} \frac{\partial^2 Z}{\partial \beta^2}, \quad \beta \equiv \frac{1}{k_B T}. \quad (4.21)$$

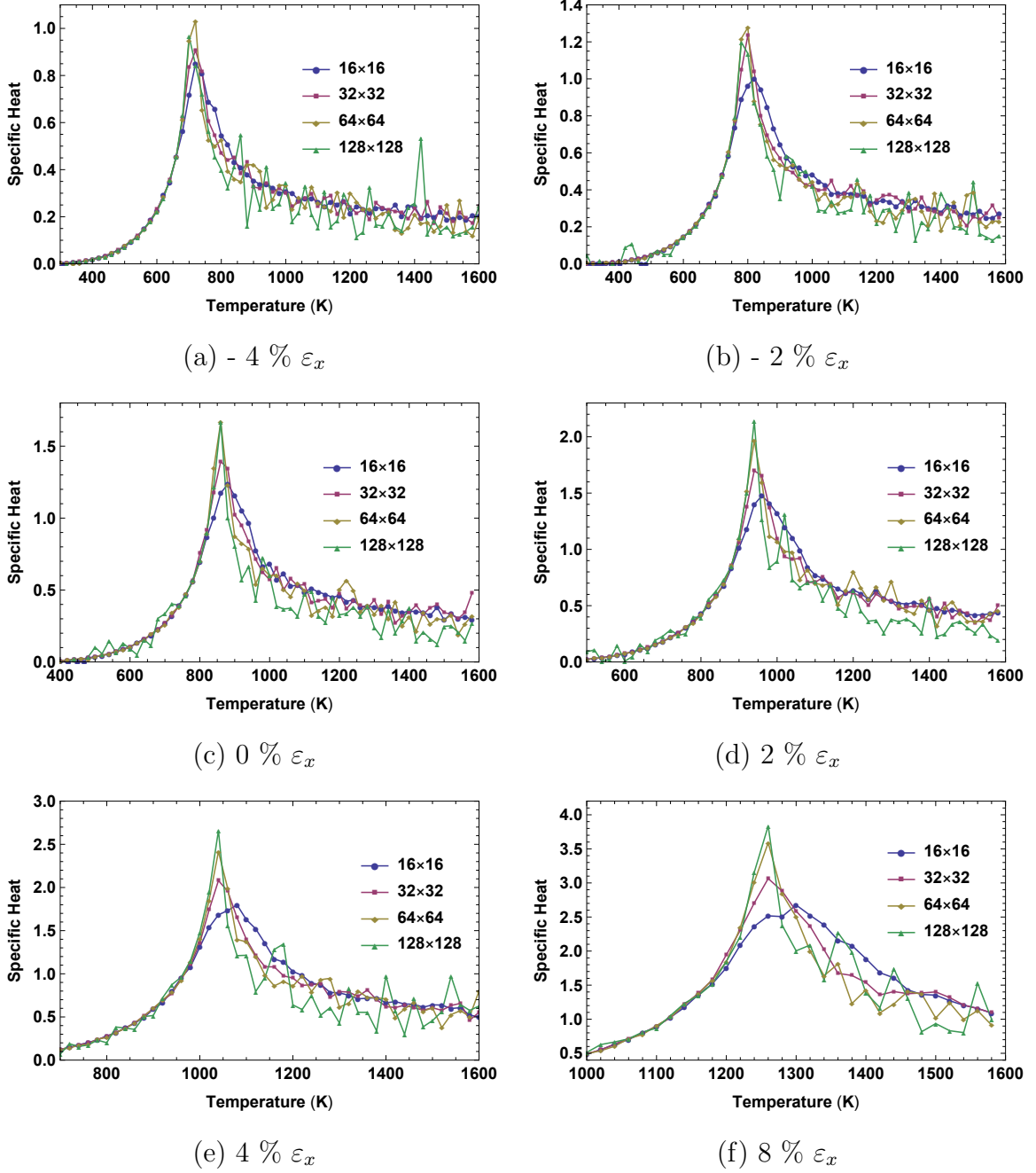


Figure 4.5: Specific heat vs. temperature for different strain values in the x direction. Critical behavior around the Curie temperature is absent because the simulations were done on finite-sized lattices.

The identities can be proven starting with the definition of the partition function, $Z = \sum e^{-\beta E_\alpha}$ and the probability $P_\alpha = \frac{e^{-\beta E_\alpha}}{Z}$ of the system being in the state with

energy E_α . Then,

$$\frac{\partial Z}{\partial \beta} = - \sum_{\alpha} E_{\alpha} e^{-\beta E_{\alpha}} = -Z \sum_{\alpha} P_{\alpha} E_{\alpha} = -Z \langle E \rangle \quad (4.22)$$

which gives the first identity from Eq. 4.21. The second identity follows similarly. Specific heat graphs are shown in figure 4.5. The system should be exhibiting divergence or critical behavior at the phase transition in the thermodynamic limit, but since simulations were done for finite size system these graphs only show a spike around the critical temperature.

4.5.3 Magnetization

Magnetization is the easiest quantity to estimate in the Ising model simulations. It is the sum of all the spins in the system,

$$M_{\alpha} = \sum_i \sigma_i \quad \text{and} \quad \langle M \rangle = \frac{1}{N} \sum_{\alpha=1}^N M_{\alpha}. \quad (4.23)$$

M_{α} is the Magnetization of a particular configuration given by the sum of spins in the configuration. Then the Monte Carlo average is simply the average of magnetizations of all the different configurations at each time-step (with N total time-steps) after the system has reached the stationary state.

Magnetization is the most interesting quantity in Ising model simulation because it is the order parameter that drops to zero at the critical temperature as seen in Figure 4.6. At the critical temperature, the system transitions from a ferromagnetic state to a paramagnetic state.

In a zero magnetic field $h = 0$, the average magnetization should be zero by symmetry, as shown in fig 4.7. In order to get the upper branch ($M/N > 0$) of the of $M(T)$ graph, we calculated the Monte Carlo average of the absolute value of the magnetization, $\langle |M| \rangle$. Results for the average absolute magnetization are shown in

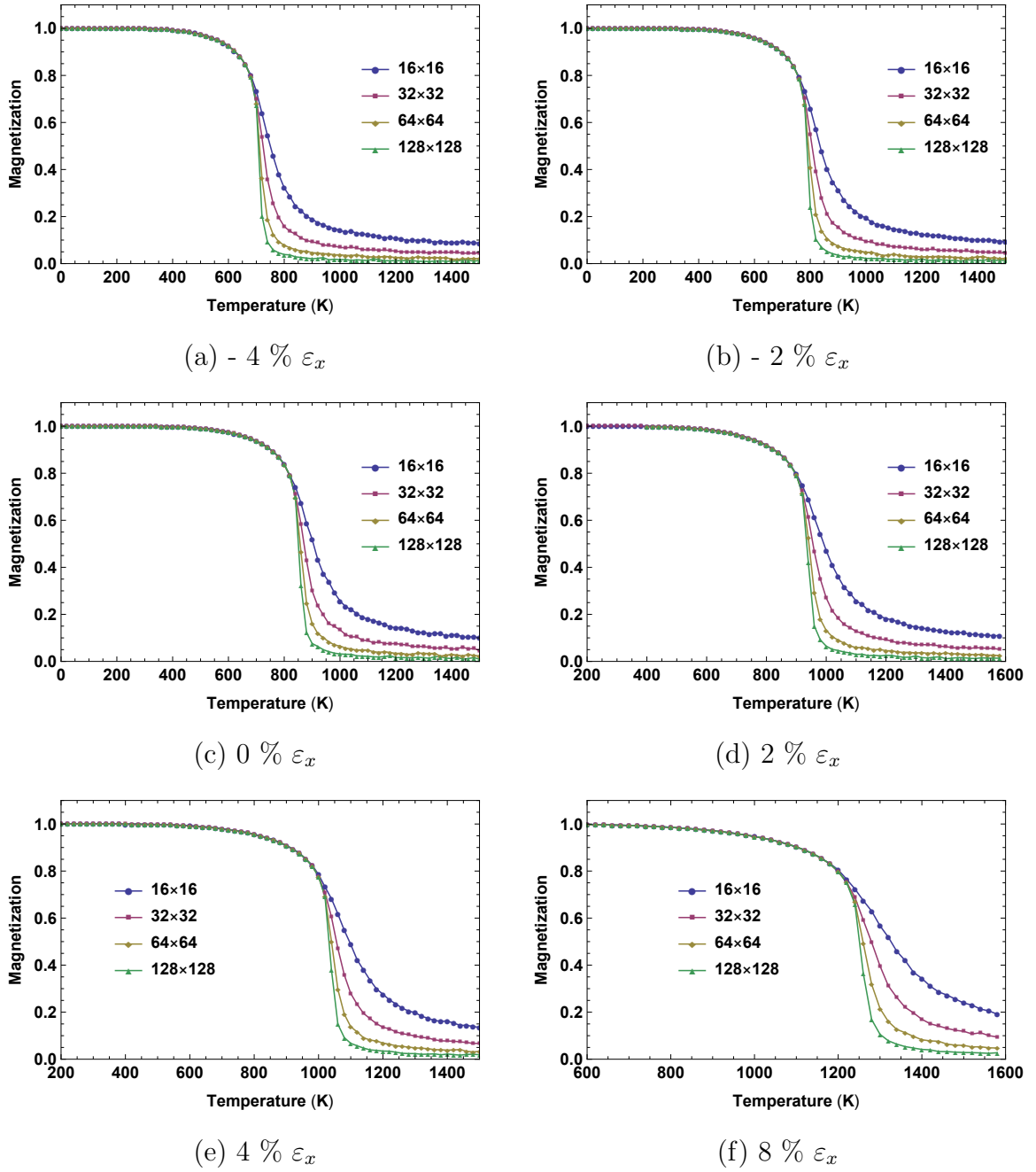


Figure 4.6: absolute Magnetization vs. temperature for different strain values in the x direction. Magnetization drops (drop becomes steeper for bigger lattice sizes and abrupt for infinitely sized lattice) to zero at the Curie temperature.

Figure 4.6.

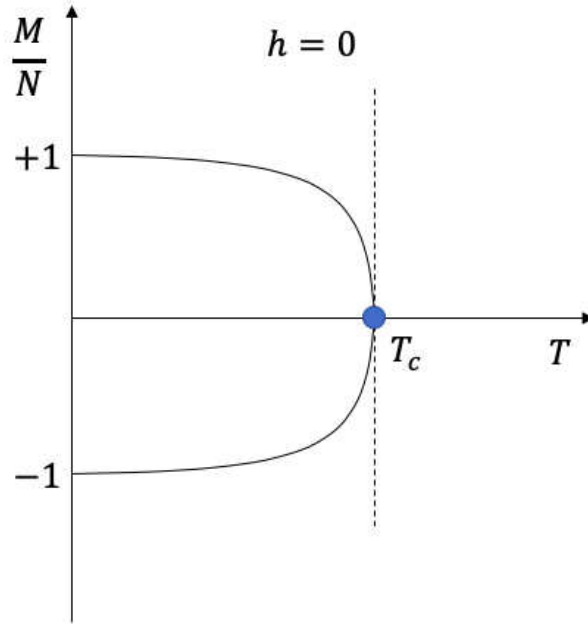


Figure 4.7: In a zero magnetic field, $h = 0$ the magnetization below the critical temperature can be either in a positive or negative direction as this is a spontaneous process.

4.5.4 Susceptibility

The magnetic susceptibility is given by differentiating the average magnetization with respect to the magnetic field. The magnetic field is set to zero after taking the derivative.

$$\chi = \left. \frac{\partial \langle M \rangle}{\partial h} \right|_{h=0}. \quad (4.24)$$

The fluctuation dissipation theorem for the susceptibility can be derived in the same manner as that for the specific heat which yields,

$$\chi = \beta [\langle M^2 \rangle - \langle M \rangle^2]. \quad (4.25)$$

The results for the magnetic susceptibility from simulations shown in fig 4.8 are actually $\chi = \beta [\langle M^2 \rangle - \langle |M| \rangle^2]$, because $\langle M \rangle = 0$ as discussed in the section 4.5.3. That is why the critical behavior (divergence at the critical temperature) that is expected for

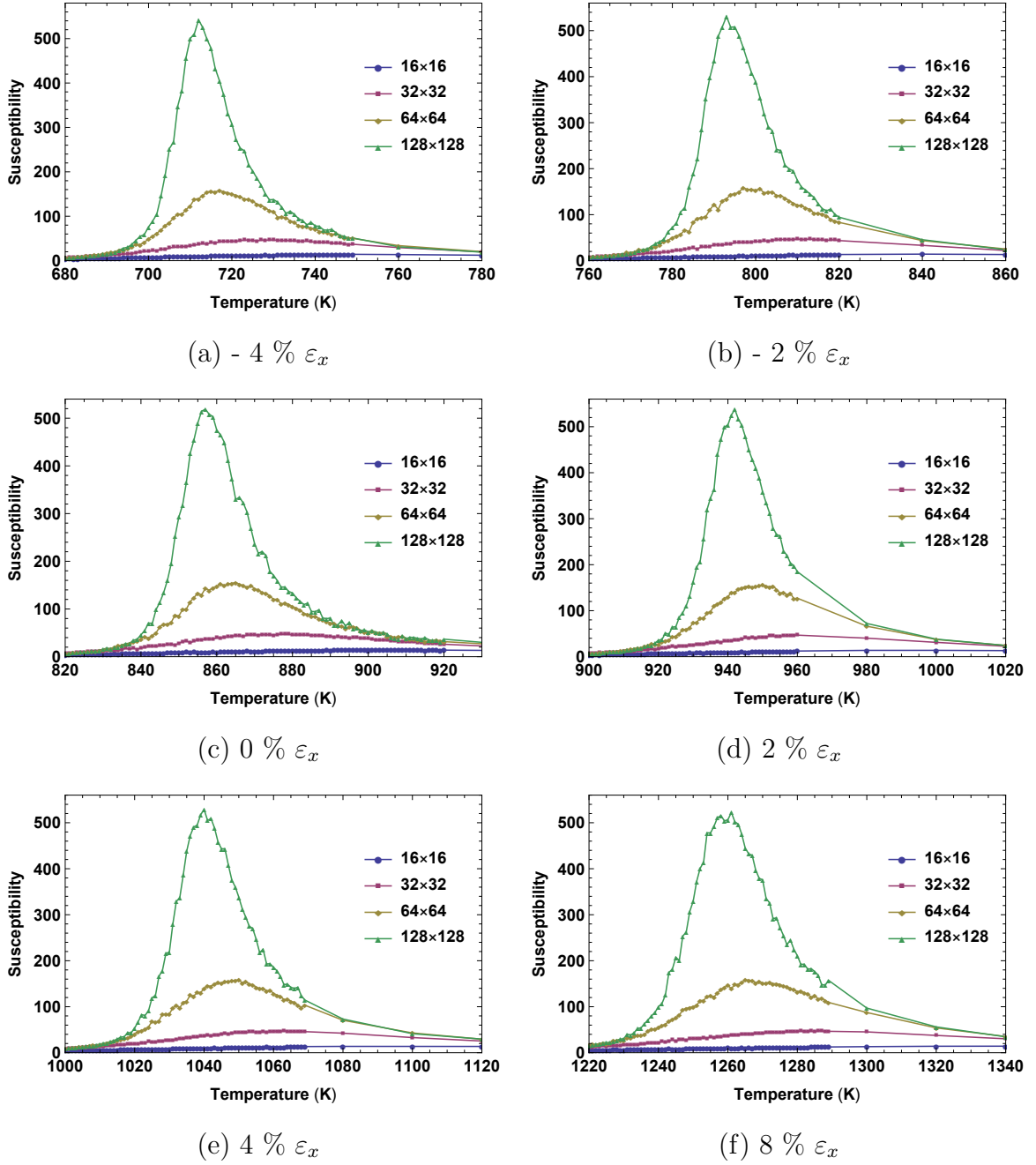


Figure 4.8: Magnetic susceptibility vs. temperature for different strain values in the x direction. Susceptibility spikes at the Curie temperature denoting a phase transition between the ferromagnetic and paramagnetic state.

the susceptibility at the phase transition is absent in the Fig. 4.8. The susceptibility is small at low temperatures because the system is in a ferromagnetic state where the spins are aligned in the same direction which makes it difficult to flip the spins with

a small external magnetic field. At high temperatures, the susceptibility is small as well, because the system is in a paramagnetic state where spins are randomized and require a high magnetic field to align them in a particular direction. Right around the Curie temperature T_c is where the susceptibility is highest because the spins are very susceptible to be influenced by the external magnetic field.

4.5.5 Binder cumulant

The Binder cumulant was calculated in order to locate T_c accurately. It is given by the following equation^{123,124},

$$U = 1 - \frac{\langle M^4 \rangle}{3\langle M^2 \rangle^2}. \quad (4.26)$$

This quantity is the fourth-order cumulant of the magnetization and is well known to have a crossing point for different lattice size simulations at the critical point T_c . The T_c obtained from the intersection point from the Binder cumulant is much more accurate than that obtained from the magnetization graph. To obtain accurate T_c from magnetization graphs the simulations must be done for much bigger lattices which have a steeper drop at the transition point. This is inefficient in terms of both simulation time and computer memory. Hence, Binder cumulant is the preferred quantity for locating T_c . The Binder cumulant graphs in fig 4.9 shows the crossing point for the different lattice sizes.

4.6 Results and conclusions

Figures 4.4, 4.5, 4.6, 4.8, and 4.9, shows results of Ising model simulations of $L \times L$ sized lattices for $L = 16, 32, 64, 128$. The energy changes concavity at the Curie temperature T_c and the specific heat spikes around that region since it related to the first derivative of the energy. The magnetization M drops to zero near the T_c , and the magnetic susceptibility is high around this region because the nature of the magnetic

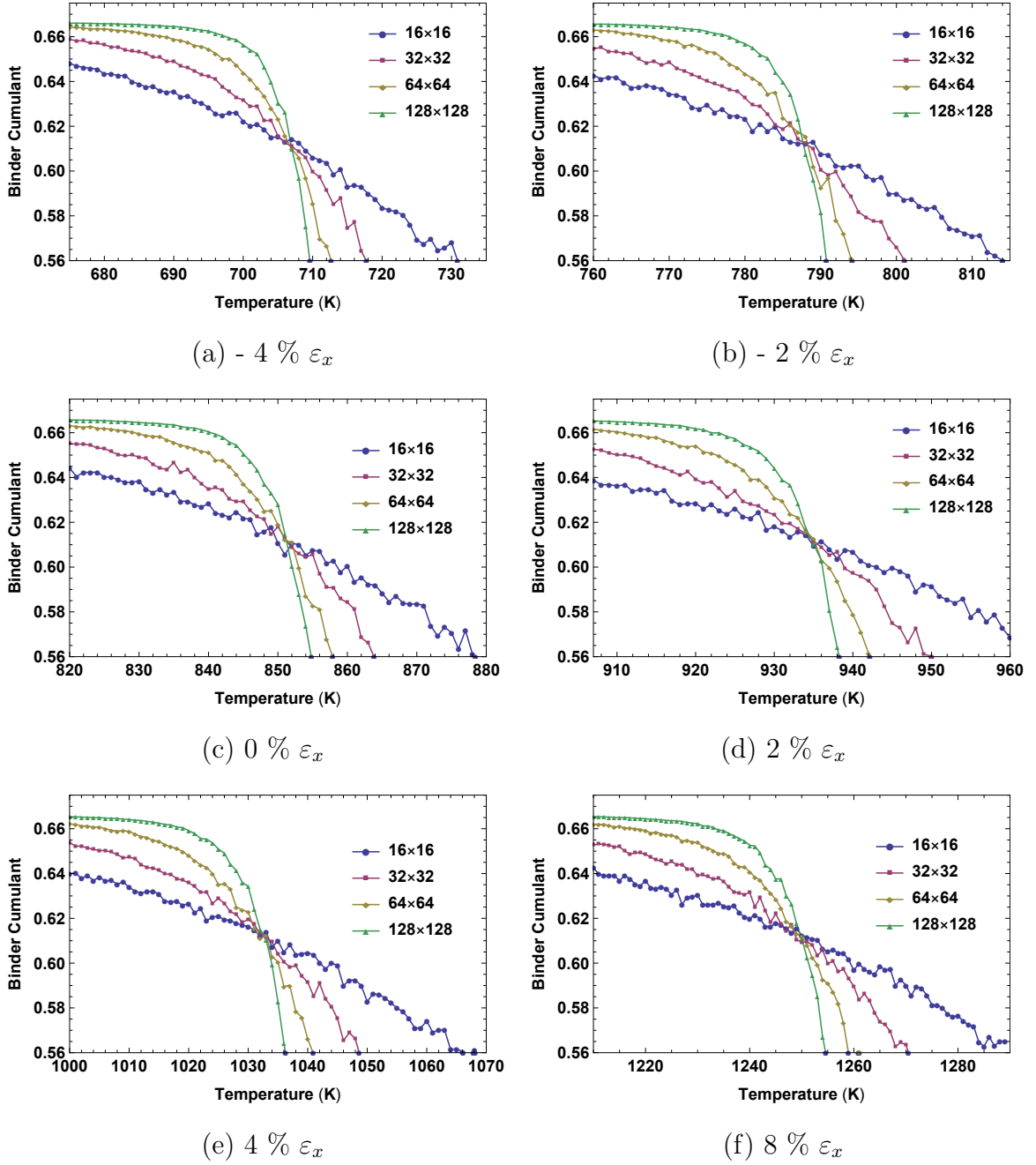
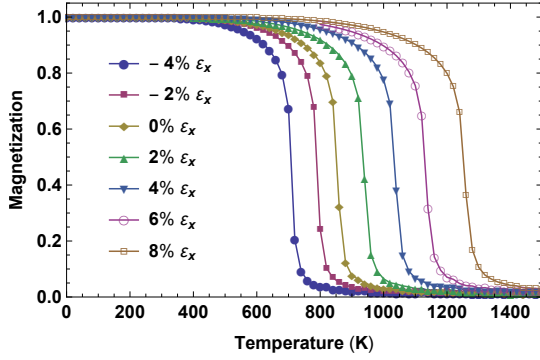
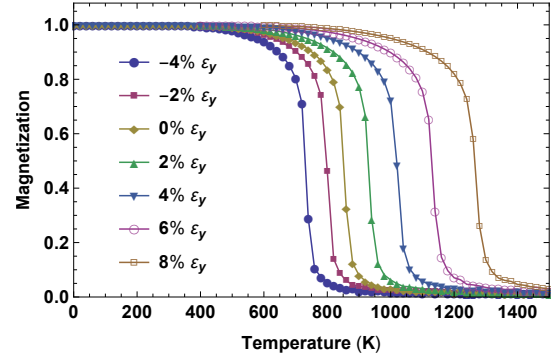


Figure 4.9: Binder cumulant vs. temperature for different strain values in the x direction. The crossing point at the critical point allows for an accurate extraction of the Curie temperature T_c . All the T_c values reported in this chapter are based on these Binder plots.

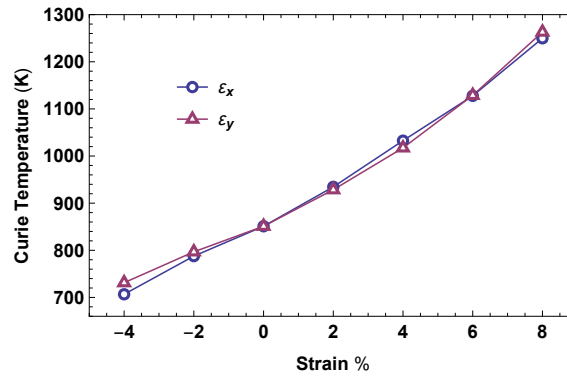
state changes around this region. The Binder cumulant has a crossing-point^{123–125} at T_c , which allows for its accurate estimation, Fig. 4.9. This quantity is the fourth



(a) Magnetization (strain in x)



(b) Magnetization (strain in y)



(c) Curie temperature vs. strain

Figure 4.10: Magnetization vs. temperature for strain in both the x (a) and y (b) direction for 128×128 triangular lattices. The Curie temperature T_c is increasing with increasing strain, which can be seen in all three graphs (a), (b), and (c). (c) There is no significant difference between how T_c increases with strain in x versus y directions.

order cumulant of the magnetization.

The most interesting result is that the T_c increases with increasing strain, as shown in Fig. 4.10(c). As illustrated by Fig. 4.10, which shows the magnetization versus temperature graph for 128×128 lattices, T_c becomes greater than 1200 K while it converts into a half-metal under uniaxial tension at higher than 7% strain in zig-zag direction and 9% strain in the armchair direction. Thus, $\text{Hf}_2\text{MnC}_2\text{O}_2$ monolayer can be transformed into an immensely useful material for spintronic applications. The computational method used for the Ising model simulation in this chapter can be

generalized to include multiple layers interacting with each other.

In the future, we are planning to find more candidate MXene monolayers that exhibit interesting electronic, magnetic, and transport properties upon application of strain or multilayering of MXene monolayers. Some of these systems might not necessarily have an easy axis that allows magnetic spins to be aligned in either parallel or anti-parallel as in an Ising model. If the spins have a three-dimensional degree of freedom then the Heisenberg model of ferromagnetism must be employed. Currently, we are working with our collaborators and actively pursuing the best course of action for the future.

CHAPTER V

SUMMARY AND DISCUSSIONS

In chapter 1, three types of random inductor-capacitor (LC) networks on 6000×6000 square lattices were simulated. The dynamical conductivity was calculated using an equation-of-motion method in which timestep error is eliminated and windowing error is minimized. The critical exponent a such that $\sigma(\omega) \propto \omega^{-a}$ was extracted at low frequencies. The results suggest that there are three different universality classes. The $L_{ij}C_i$ model, with capacitances from each site to ground, has $a = 0.314(4)$. The $L_{ij}C_{ij}$ model, with capacitances along bonds, has $a = 0$. The $L_{ij}C_iC_{ij}$ model, with both types of capacitances, has $a = 0.304(1)$. This implies that classical percolative 2D superconductor-insulator transitions (SITs) generically have $\sigma(\omega) \rightarrow \infty$ as $\omega \rightarrow 0$. Therefore, any experiments that give a constant conductivity as $\omega \rightarrow 0$ must be explained in terms of quantum effects.

In chapter 3, simulations of a quantum rotor model describing a Josephson junction array (JJA) in the phase representation at zero temperature in a perpendicular magnetic field $B = 0.1, 0.2, 0.3, 0.4$ (in units of $\hbar/2ea^2$) on a $L \times L$ square lattice with spacing a for $L = 6, 8, 10, 12$ was presented. The superconductor-insulator transition (SIT) is tuned by the ratio of charging energy to Josephson coupling, U/J . Abrupt drops in the magnetization values were observed in the bigger lattices at certain values of B and U/J caused by the formation of vortices. Increasing U/J at a fixed B field causes quantum vortex melting. The magnetization drops to zero around $U/J \simeq 5$ indicating SIT. For $B = 0.1$ the SIT occurs without an intermediate vortex state and the magnetization scales as $M \sim L^4$, whereas for $B = 0.4$ the scaling is $M \sim L^2$ dur-

ing the vortex melting. For B between 0.1 and 0.4 the scaling is not clear. We used the diffusion Monte Carlo (DMC) method with a guiding wavefunction optimized using the variational Monte Carlo (VMC) method. We developed the DMC and VMC algorithms for JJAs and implemented them in C++ . The ground state energy is calculated easily in DMC and its error estimates were generally smaller than 1%, both with and without the guiding wavefunction. Quantities like magnetization and vorticity that do not commute with the Hamiltonian were calculated using an efficient forward walking algorithm. Their estimates are affected severely in absence of the guiding wavefunction. With the guiding wavefunction, errors for the magnetization were generally less than 1% and going up to 15% percent around the phase transition from the Meissner to the vortex state, and without the guiding wavefunction errors were generally higher than 5% and going up to 40% around the critical point.

In chapter 3, Curie temperatures for a MXene monolayer $\text{Hf}_2\text{MnC}_2\text{O}_2$ under different strain values were calculated using an anisotropic Ising model. This material exhibits a semiconductor to a half-metal transition at 7% strain applied in the zigzag direction and at 9% strain applied in the armchair direction. Also, a semiconductor-to-metal transition is predicted for this monolayer at 4% compressive strain in either direction. Calculations from Ising model simulations show that the Curie temperature of the material can be enhanced significantly by applying tensile strain. For example, at 8% strain, the Curie temperature becomes greater than 1200 K.

APPENDICES

A1 Details of algorithms for LC network models

A1.1 Algorithm for the $L_{ij}C_iC_{ij}$ Model

For implementation purposes we let I_{xy}^X be the current flowing from site (x, y) to $(x + 1, y)$, I_{xy}^Y be the current flowing from site (x, y) to $(x, y + 1)$, and similarly for the U variables. The initial currents (at time $t = 0$) and voltages (at $t = \tau/2$) are

$$I_{xy}^X := \frac{1}{L_{xy}^X}$$

$$I_{xy}^Y := 0$$

$$U_{xy}^X := \frac{\tau}{2C_{xy}^X} I_{xy}^X$$

$$U_{xy}^Y := \frac{\tau}{2C_{xy}^Y} I_{xy}^Y$$

$$V_{xy} := \frac{\tau}{2C_{xy}} (I_{x-1,y}^X - I_{xy}^X + I_{x,y-1}^Y - I_{xy}^Y).$$

The currents and voltages at later times are then computed using the leapfrog algorithm,

$$\begin{aligned}
I_{xy}^X & += \frac{\tau}{L_{xy}^X} (V_{xy} - V_{x+1,y} - U_{xy}^X) \\
I_{xy}^Y & += \frac{\tau}{L_{xy}^Y} (V_{xy} - V_{x,y+1} - U_{xy}^Y) \\
U_{xy}^X & += \frac{\tau}{C_{xy}^X} I_{xy}^X \\
U_{xy}^Y & += \frac{\tau}{C_{xy}^Y} I_{xy}^Y \\
V_{xy} & += \frac{\tau}{C_{xy}} (I_{x-1,y}^X - I_{xy}^X + I_{x,y-1}^Y - I_{xy}^Y)
\end{aligned} \tag{A.1}$$

where += is the increment operator as in the C language.

The $L_{ij}C_i$ model can be simulated using similar approach.

A1.2 Algorithm for the $L_{ij}C_{ij}$ Model

For $C_i = 0$, Eq. (2.9) becomes pathological because Kirchhoff's current law applies as a hard constraint at every site:¹

$$\sum_{j@i} I_{ij} = 0. \tag{A.2}$$

¹The situation is analogous to incompressible fluid dynamics described by the Navier-Stokes equation, where the incompressibility constraint must be incorporated at every timestep by solving Poisson's equation.

Differentiating by t and using Eq. (2.9) gives

$$\sum_{j @ i} \frac{V_i - V_j}{L_{ij}} = \sum_{j @ i} \frac{U_{ij}}{L_{ij}}. \quad (\text{A.3})$$

On a square lattice with periodic boundary conditions with identical inductances $L_{xy}^X = L_{xy}^Y = 1$ for all (x, y) , this leads to the lattice Poisson equation,

$$\begin{aligned} 4V_{xy} - (V_{x+1,y} + V_{x-1,y} + V_{x,y+1} + V_{x,y-1}) \\ = U_{xy}^X - U_{x-1,y}^X + U_{xy}^Y - U_{x,y-1}^Y \equiv J_{xy}, \end{aligned} \quad (\text{A.4})$$

which can be solved efficiently using fast Fourier transform methods. We summarize the algorithm below.

The momentum-space Green function is precalculated as $\tilde{G}_{pq} = (4 \sin^2 \frac{\pi p}{N_x} + 4 \sin^2 \frac{\pi q}{N_y})^{-1}$ for $p = 0, 1, 2, \dots, N_x - 1$ and $q = 0, 1, 2, \dots, N_y - 1$ and regularized such that $\tilde{G}_{00} = 0$. The initial currents and voltages are

$$\begin{aligned} I_{xy}^X &:= 1 \\ I_{xy}^Y &:= 0 \\ U_{xy}^X &:= \frac{\tau}{2C_{xy}^X} I_{xy}^X \\ U_{xy}^Y &:= \frac{\tau}{2C_{xy}^Y} I_{xy}^Y. \end{aligned} \quad (\text{A.5})$$

The system is evolved using

$$J_{xy} := U_{xy}^X - U_{x-1,y}^X + U_{xy}^Y - U_{x,y-1}^Y \quad (\text{A.6})$$

$$\tilde{J}_{pq} := \frac{1}{\sqrt{N_x N_y}} \sum_{xy} e^{-2\pi i(px/N_x + qy/N_y)} J_{xy} \quad (\text{A.7})$$

$$\tilde{V}_{pq} := \tilde{G}_{pq} \tilde{J}_{pq} \quad (\text{A.8})$$

$$V_{pq} := \frac{1}{\sqrt{N_x N_y}} \sum_{xy} e^{2\pi i(px/N_x + qy/N_y)} \tilde{V}_{pq} \quad (\text{A.9})$$

$$I_{xy}^X += \frac{\tau}{L_{xy}^X} (V_{xy} - V_{x+1,y} - U_{xy}^X) \quad (\text{A.10})$$

$$I_{xy}^Y += \frac{\tau}{L_{xy}^Y} (V_{xy} - V_{x,y+1} - U_{xy}^Y) \quad (\text{A.11})$$

$$U_{xy}^X += \frac{\tau}{C_{xy}^X} I_{xy}^X \quad (\text{A.12})$$

$$U_{xy}^Y += \frac{\tau}{C_{xy}^Y} I_{xy}^Y \quad (\text{A.13})$$

where Eqs. (A.7) and (A.9) are implemented as two-dimensional fast Fourier transforms.

A1.3 Maximum frequency in the $L_{ij}C_iC_{ij}$ model

The maximum timesteps in the LC network models are limited by the maximum frequency of the current in the lattice, $\tau_{\max} < 2/\omega_{\max}$. The maximum frequency ω_{\max} is given by the biggest frequency eigenmode. Rewriting the Eq. (A.1) after Fourier

transform,

$$-i\omega \underbrace{\begin{pmatrix} L & 0 & 0 & 0 & 0 \\ 0 & L & 0 & 0 & 0 \\ 0 & 0 & C_2 & 0 & 0 \\ 0 & 0 & 0 & C_2 & 0 \\ 0 & 0 & 0 & 0 & C_1 \end{pmatrix}}_{\mathbf{M}} \underbrace{\begin{pmatrix} I_{q_x} \\ I_{q_y} \\ I_{q_x} \\ I_{q_y} \\ V_q \end{pmatrix}}_{\mathbf{H}} = \underbrace{\begin{pmatrix} 0 & 0 & -1 & 0 & 1 - e^{iq_x} \\ 0 & 0 & 0 & -1 & 1 - e^{iq_y} \\ 1 & 0 & 0 & 0 & 0 \\ 0 & 1 & 0 & 0 & 0 \\ e^{-iq_x} - 1 & e^{-iq_y} - 1 & 0 & 0 & 0 \end{pmatrix}}_{\mathbf{H}} \begin{pmatrix} I_{q_x} \\ I_{q_y} \\ I_{q_x} \\ I_{q_y} \\ V_q \end{pmatrix},$$

where $(L_{xy}^X, L_{xy}^Y) = L$, $(C_{xy}^X, C_{xy}^Y) = C_2$, and $C_{xy} = C_1$. Eigenvalues of matrix $-i\sqrt{\mathbf{M}^{-1}\mathbf{H}\sqrt{\mathbf{M}^{-1}}}$ are

$$0, \pm \frac{1}{\sqrt{LC_2}}, \pm \underbrace{\sqrt{\frac{C_1 + 4C_2(\sin^2(\frac{q_x}{2}) + \sin^2(\frac{q_y}{2}))}{LC_1C_2}}}_{\omega_0}.$$

The relevant frequency eigenmode is ω_0 and the maximum frequency ω_{\max} is given by ω_0 when the sine terms in it are equal to one,

$$\omega_{\max} = \sqrt{\frac{C_1 + 8C_2}{LC_1C_2}}. \quad (\text{A.14})$$

The maximum allowed timestep for the simulation to be stable is $\tau_{\max} = 2/\omega_{\max}$, which can be calculated for different values of L , C_1 , and C_2 using Eq. (A.14).

A2 Derivation of Josephson equations

With $\psi_i = \sqrt{n_i}e^{i\theta_i}$, its time derivative is

$$\frac{\partial\psi}{\partial t} = \dot{\psi}_i = \frac{1}{2\sqrt{n_i}}\dot{n}_i e^{i\theta_i} + i\sqrt{n_i}\dot{\theta}_i e^{i\theta_i}. \quad (\text{A.15})$$

Substituting ψ and $\dot{\psi}$ into the coupled Schrödinger's equations in Eq. (3.2) gives,

$$\begin{aligned} i\frac{\dot{n}_1}{2\sqrt{n_1}} - \sqrt{n_1}\dot{\theta}_1 &= U_1\sqrt{n_1} + \alpha\sqrt{n_2}e^{i(\theta_2-\theta_1)} \\ i\frac{\dot{n}_2}{2\sqrt{n_2}} - \sqrt{n_2}\dot{\theta}_2 &= U_2\sqrt{n_2} + \alpha\sqrt{n_1}e^{i(\theta_1-\theta_2)}. \end{aligned} \quad (\text{A.16})$$

Using the fact that $\dot{n}_1 = -\dot{n}_2$, since a charge lost by one superconductor is gained by another. Also, taking the real part of the Eq. (A.16) gives,

$$-\dot{n}_1 = 2\alpha\sqrt{n_1 n_2} \sin(\theta_1 - \theta_2), \quad (\text{A.17})$$

which is the rate of charges moving from one superconductor to another. Therefore, the current is given by $I_{12} = -e_*\dot{n}_1 = 2e_*\alpha\sqrt{n_1 n_2} \sin(\theta_1 - \theta_2) = I_c \sin(\theta_1 - \theta_2)$.

Taking the imaginary part of the Eq. (A.16) gives,

$$-\sqrt{n_1}\dot{\theta}_1 = E_1\sqrt{n_1} + \alpha\sqrt{n_2} \cos(\theta_2 - \theta_1) \quad (\text{A.18})$$

$$-\sqrt{n_2}\dot{\theta}_2 = E_2\sqrt{n_2} + \alpha\sqrt{n_1} \cos(\theta_1 - \theta_2). \quad (\text{A.19})$$

Since $n_1 \simeq n_2$ (good approximation for identical coupled superconductors), subtracting Eq. (A.19) from Eq. (A.18) yields,

$$\dot{\theta} = \dot{\theta}_1 - \dot{\theta}_2 = U_1 - U_2 = e_c V, \quad (\text{A.20})$$

which is Josephson's second equation.

A3 Detailed derivations of some quantities in DMC method

A3.1 Expanding a term from equation (3.20)

The first term in the RHS of equation (3.20) can be expanded as follows,

$$\begin{aligned} \Psi_G \nabla^2 \left(\frac{f}{\Psi_G} \right) &= \Psi_G \nabla \cdot \left(\frac{\Psi_G \nabla f - f \nabla \Psi_G}{\Psi_G^2} \right) \\ &= \Psi_G \nabla \cdot \left(\frac{\nabla f}{\Psi_G} \right) - \Psi_G \nabla \cdot \left(\frac{f \nabla \Psi_G}{\Psi_G^2} \right) \\ &= \nabla^2 f + \Psi_G \nabla \cdot \left(\frac{1}{\Psi_G} \right) \cdot \nabla f - \frac{1}{\Psi_G} \nabla \cdot (f \nabla \Psi_G) - f \Psi_G \nabla \cdot \left(\frac{1}{\Psi_G^2} \right) \cdot \nabla \Psi_G \\ &= \nabla^2 f - \frac{1}{\Psi_G} \nabla f \cdot \nabla \Psi_G - \frac{1}{\Psi_G} \nabla f \cdot \nabla \Psi_G - \frac{\nabla^2 \Psi_G}{\Psi_G} f + \frac{2f}{\Psi_G^2} \nabla \Psi_G \cdot \nabla \Psi_G \\ &= \nabla^2 f - \frac{2}{\Psi_G} \nabla f \cdot \nabla \Psi_G - 2 \frac{\nabla^2 \Psi_G}{\Psi_G} f + \frac{\nabla^2 \Psi_G}{\Psi_G} f + \frac{2f}{\Psi_G^2} |\nabla \Psi_G|^2 \\ &= \nabla^2 f + \left(\frac{\nabla^2 \Psi_G}{\Psi_G} \right) f - \frac{2}{\Psi_G} \nabla f \cdot \nabla \Psi_G - 2 \frac{\nabla^2 \Psi_G}{\Psi_G} - 2f \nabla \cdot \left(\frac{1}{\Psi_G} \right) \cdot \nabla \Psi_G \\ &= \nabla^2 f + \left(\frac{\nabla^2 \Psi_G}{\Psi_G} \right) f - 2 \left(f \nabla \cdot \frac{\nabla \Psi_G}{\Psi_G} + \nabla f \cdot \frac{\nabla \Psi_G}{\Psi_G} \right) \\ &= \nabla^2 f - 2 \nabla \cdot \left(\frac{\nabla \Psi_G}{\Psi_G} f \right) + \left(\frac{\nabla^2 \Psi_G}{\Psi_G} \right) f. \end{aligned}$$

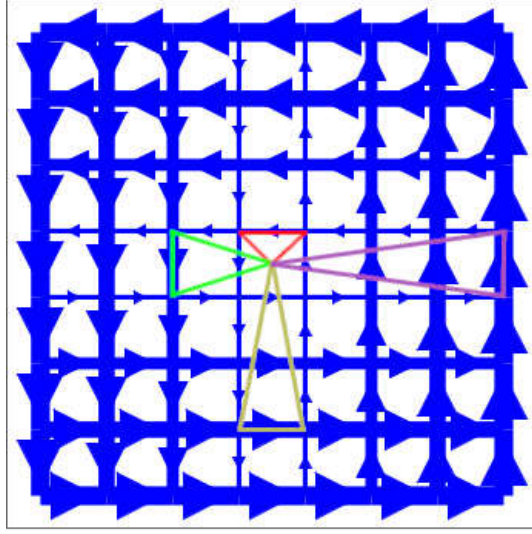


Figure A.1: Magnetic vector potential in a constant perpendicular magnetic field in a symmetric gauge.

These three terms eventually lead the Schrödinger's equation for the DMC algorithm to an equation resembling a Fickian diffusion equation with an extra term (growth or decay term).

A3.2 The magnetic vector potential A in a constant perpendicular B field

Geometrically the magnetic vector potential represents the area of a triangle with vertices $(0, 0)$, (x_i, y_i) , and (x_j, y_j) , which is the reason its value increases away from the center of the lattice as shown in fig A.1. Parametrizing the path as $\mathbf{r} = \mathbf{r}_i +$

$\lambda(\mathbf{r}_j - \mathbf{r}_i)$ continuously from grain i to grain j , with $0 \leq \lambda \leq 1$:

$$\begin{aligned}
A_{ij} &= \frac{2e}{\hbar c} \int_{\mathbf{r}_i}^{\mathbf{r}_j} \mathbf{A}(\mathbf{r}) \cdot d\mathbf{r} \\
&= \frac{2e}{\hbar c} \int_0^1 \left(\frac{1}{2} \mathbf{B} \times [\mathbf{r}_i + \lambda(\mathbf{r}_j - \mathbf{r}_i)] \right) \cdot d\lambda(\mathbf{r}_j - \mathbf{r}_i) \\
&= \frac{2e}{\hbar c} \left(\frac{1}{2} \mathbf{B} \times \left[\mathbf{r}_i + (\mathbf{r}_j - \mathbf{r}_i) \int_0^1 \lambda d\lambda \right] \right) \cdot (\mathbf{r}_j - \mathbf{r}_i) \\
&= \frac{2e}{\hbar c} \left(\frac{1}{2} \mathbf{B} \times \frac{1}{2} (\mathbf{r}_j + \mathbf{r}_i) \right) \cdot (\mathbf{r}_j - \mathbf{r}_i) \\
&= \frac{2e B_0}{\hbar c} \frac{1}{4} [-(y_i + y_j)\hat{i} + (x_i + x_j)\hat{j}] \cdot [(x_j - x_i)\hat{i} + (y_j - y_i)\hat{j}] \\
\therefore A_{ij} &= \frac{2e B_0}{\hbar c} \frac{1}{2} (x_i y_j - x_j y_i).
\end{aligned}$$

A3.3 Derivation of the drift velocity

Starting with the definition of the drift velocity $\mathbf{v}(\mathbf{r}) = U \frac{\nabla \Psi_G}{\Psi_G}$ and the chosen guiding wavefunction of $\Psi_G(\boldsymbol{\theta}) = \exp \left[\sum_{\langle ij \rangle} K \cos(\theta_i - \theta_j - A_{ij}) \right]$ gives,

$$\begin{aligned}
v_i &= U \frac{\partial_{\theta_i} \Psi}{\Psi} \\
&= U \frac{\partial}{\partial \theta_i} \sum_{\langle ij \rangle} K \cos(\theta_j - \theta_k - A_{jk}) \\
&= U \sum_{\langle ij \rangle} K \sin(\theta_k - \theta_j - A_{kj}) (\delta_{ij} - \delta_{ik}) \\
&= \frac{U}{2} \left[\sum_j \sum_k K_{jk} \sin(\theta_k - \theta_j - A_{kj}) \delta_{ij} - \sum_j \sum_k K_{jk} \sin(\theta_k - \theta_j - A_{kj}) \delta_{ik} \right] \\
&= \frac{U}{2} \left[\sum_k K_{ik} \sin(\theta_k - \theta_i - A_{ki}) + \sum_j K_{ij} \sin(\theta_j - \theta_i - A_{ji}) \right] \\
&= \frac{U}{2} \left[\sum_j K_{ij} \sin(\theta_j - \theta_i - A_{ji}) + \sum_j K_{ij} \sin(\theta_j - \theta_i - A_{ji}) \right] \\
&= U \sum_{j @ i} K \sin(\theta_j - \theta_i - A_{ji}).
\end{aligned}$$

REFERENCES

- [1] P. Karki and Y. L. Loh, *Journal of Physics: Condensed Matter* **28**, 435701 (2016).
- [2] Y. L. Loh and P. Karki, *Journal of Physics: Condensed Matter* **29**, 425901 (2017).
- [3] P. Karki and Y. L. Loh, *Journal of Physics: Condensed Matter* **30**, 385901 (2018).
- [4] E. M. D. Siriwardane, P. Karki, Y. L. Loh, and D. Çakır, *The Journal of Physical Chemistry C* **123**, 12451 (2019).
- [5] W. Meissner and R. Ochsenfeld, *Naturwissenschaften* **21**, 787 (1933).
- [6] F. London, H. London, and F. A. Lindemann, *Proceedings of the Royal Society of London. Series A - Mathematical and Physical Sciences* **149**, 71 (1935).
- [7] D. Shoenberg, *Nature* **143**, 434 (1939).
- [8] A. B. Pippard and W. L. Bragg, *Proceedings of the Royal Society of London. Series A. Mathematical and Physical Sciences* **191**, 370 (1947).
- [9] E. Maxwell, *Phys. Rev.* **78**, 477 (1950).
- [10] C. A. Reynolds, B. Serin, W. H. Wright, and L. B. Nesbitt, *Phys. Rev.* **78**, 487 (1950).
- [11] H. Fröhlich, *Phys. Rev.* **79**, 845 (1950).

- [12] V. L. Ginzburg and L. D. Landau, Zh. Eksp. Teor. Fiz. **20**, 1064 (1950).
- [13] A. A. Abrikosov, Sov. Phys. JETP **5**, 1174 (1957), [Zh. Eksp. Teor. Fiz.32,1442(1957)].
- [14] J. Bardeen, L. N. Cooper, and J. R. Schrieffer, Phys. Rev. **108**, 1175 (1957).
- [15] L. Gor'kov, Sov. Phys. - JETP (Engl. Transl.); (United States) .
- [16] I. Giaever, Phys. Rev. Lett. **5**, 147 (1960).
- [17] J. Nicol, S. Shapiro, and P. H. Smith, Phys. Rev. Lett. **5**, 461 (1960).
- [18] J. Bardeen, Phys. Rev. Lett. **7**, 162 (1961).
- [19] B. Josephson, Physics Letters **1**, 251 (1962), ISSN 0031-9163.
- [20] P. Adams, Phys. Rev. Lett. **92**, 067003 (2004).
- [21] A. F. Hebard and M. A. Paalanen, Phys. Rev. Lett. **65**, 927 (1990).
- [22] D. B. Haviland, Y. Liu, and A. M. Goldman, PRL **62**, 2180 (1989).
- [23] A. T. Bollinger, G. Dubuis, J. Yoon, D. Pavuna, J. Misewich, and I. Bozovic, Nature **472**, 458 (2011), ISSN 0028-0836.
- [24] Y. Lee, C. Clement, J. Hellerstedt, J. Kinney, L. Kinnischtzke, X. Leng, S. D. Snyder, and A. M. Goldman, Phys. Rev. Lett. **106**, 136809 (2011).
- [25] E. Granato, Journal of Physics: Conference Series **568**, 022017 (2014).
- [26] W. LENZ, Phys. Zs. **21**, 613 (1920).
- [27] E. Ising, Z. Phys. **31**, 253 (1925).
- [28] R. Peierls and M. Born, Proceedings of the Cambridge Philosophical Society **32**, 477 (1936).

- [29] H. A. Kramers and G. H. Wannier, Phys. Rev. **60**, 252 (1941).
- [30] H. A. Kramers and G. H. Wannier, Phys. Rev. **60**, 263 (1941).
- [31] L. Onsager, Phys. Rev. **65**, 117 (1944).
- [32] P. Kasteleyn, Physica **27**, 1209 (1961), ISSN 0031-8914.
- [33] C. A. Hurst and H. S. Green, jcp **33**, 1059 (1960).
- [34] M. E. Fisher, Phys. Rev. **124**, 1664 (1961).
- [35] M. Kac and J. C. Ward, Phys. Rev. **88**, 1332 (1952).
- [36] A. Goldman and N. Markovic, Physics Today **51**, 39 (1998).
- [37] V. F. Gantmakher and V. T. Dolgoplov, Physics-Uspekhi **53**, 3 (2010).
- [38] D. Shahar and Z. Ovadyahu, Phys. Rev. B **46**, 10917 (1992).
- [39] M. A. Steiner, G. Boebinger, and A. Kapitulnik, Phys. Rev. Lett. **94**, 107008 (2005).
- [40] M. D. Stewart, A. Yin, J. M. Xu, and J. M. Valles, Science **318**, 1273 (2007).
- [41] I. Hetel, T. R. Lemberger, and M. Randeria, Nat. Phys. **3**, 700 (2007), ISSN 1745-2473.
- [42] W. Liu, M. Kim, G. Sambandamurthy, and N. P. Armitage, Phys. Rev. B **84**, 024511 (2011).
- [43] T. Hofmann, C. M. Herzinger, A. Boosalis, T. E. Tiwald, J. A. Woollam, and M. Schubert, Review of Scientific Instruments **81**, 023101 (2010), ISSN 00346748.

- [44] R. Valdés Aguilar, L. S. Bilbro, S. Lee, C. W. Bark, J. Jiang, J. D. Weiss, E. E. Hellstrom, D. C. Larbalestier, C. B. Eom, and N. P. Armitage, *Phys. Rev. B* **82**, 180514 (2010).
- [45] M. Mondal, A. Kamalpure, S. C. Ganguli, J. Jesudasan, V. Bagwe, L. Benfatto, and P. Raychaudhuri, *Sci. Rep.* **3**, 1357 (2013).
- [46] A. M. Finkel'stein, *Physica B* **197**, 636 (1994).
- [47] M. P. A. Fisher, G. Grinstein, and S. M. Girvin, *PRL* **64**, 587 (1990).
- [48] M.-C. Cha, M. P. A. Fisher, S. M. Girvin, M. Wallin, and A. P. Young, *Phys. Rev. B* **44**, 6883 (1991).
- [49] E. S. Sørensen, M. Wallin, S. M. Girvin, and A. P. Young, *Phys. Rev. Lett.* **69**, 828 (1992).
- [50] K. J. Runge, *Phys. Rev. B* **45**, 13136 (1992).
- [51] M. Makivić, N. Trivedi, and S. Ullah, *Phys. Rev. Lett.* **71**, 2307 (1993).
- [52] G. G. Batrouni, B. Larson, R. T. Scalettar, J. Tobochnik, and J. Wang, *Phys. Rev. B* **48**, 9628 (1993).
- [53] M.-C. Cha and S. M. Girvin, *Phys. Rev. B* **49**, 9794 (1994).
- [54] J. Šmakov and E. Sørensen, *Phys. Rev. Lett.* **95**, 180603 (2005).
- [55] F. Lin, E. S. Sørensen, and D. M. Ceperley, *Phys. Rev. B* **84**, 094507 (2011).
- [56] S. Sachdev, *Quantum Phase Transitions* (Cambridge, London, 1999).
- [57] D. Stroud, *Physica A: Statistical Mechanics and its Applications* **207**, 280 (1994), ISSN 0378-4371.

- [58] S. Gazit, D. Podolsky, A. Auerbach, and D. P. Arovas, *Phys. Rev. B* **88**, 235108 (2013).
- [59] W. Witczak-Krempa, E. S. Sørensen, and S. Sachdev, *Nat. Phys.* **10**, 361 (2014), ISSN 5.
- [60] K. Chen, L. Liu, Y. Deng, L. Pollet, and N. Prokof'ev, *Phys. Rev. Lett.* **112**, 030402 (2014).
- [61] M. Swanson, Y. L. Loh, M. Randeria, and N. Trivedi, *Phys. Rev. X* **4**, 021007 (2014).
- [62] Y. L. Loh, R. Dhakal, J. F. Neis, and E. M. Moen, *Journal of Physics: Condensed Matter* **26**, 505702 (2014).
- [63] D. M. Ceperley and B. J. Alder, *Phys. Rev. Lett.* **45**, 566 (1980).
- [64] C. Attaccalite, S. Moroni, P. Gori-Giorgi, and G. B. Bachelet, *Phys. Rev. Lett.* **88**, 256601 (2002).
- [65] M. Holzmann, B. Bernu, and D. M. Ceperley, *Phys. Rev. B* **74**, 104510 (2006).
- [66] J. Carlson and S. Reddy, *Phys. Rev. Lett.* **100**, 150403 (2008).
- [67] C. Filippi, S. B. Healy, P. Kratzer, E. Pehlke, and M. Scheffler, *Phys. Rev. Lett.* **89**, 166102 (2002).
- [68] A. J. Williamson, R. Q. Hood, R. J. Needs, and G. Rajagopal, *Phys. Rev. B* **57**, 12140 (1998).
- [69] N. D. Drummond, A. J. Williamson, R. J. Needs, and G. Galli, *Phys. Rev. Lett.* **95**, 096801 (2005).
- [70] D. Alfè and M. J. Gillan, *Phys. Rev. B* **71**, 220101 (2005).

- [71] R. Maezono, A. Ma, M. D. Towler, and R. J. Needs, Phys. Rev. Lett. **98**, 025701 (2007).
- [72] J. Yu, L. K. Wagner, and E. Ertekin **143**, 224707 (2015).
- [73] C. Mitra, J. T. Krogel, J. A. Santana, and F. A. Reboredo **143**, 164710 (2015).
- [74] L. Mitáš, E. L. Shirley, and D. M. Ceperley **95**, 3467 (1991).
- [75] J. A. Santana, J. T. Krogel, P. R. C. Kent, and F. A. Reboredo **144**, 174707 (2016).
- [76] J. A. Santana, J. T. Krogel, J. Kim, P. R. C. Kent, and F. A. Reboredo **142**, 164705 (2015).
- [77] L. K. Wagner **19**, 343201 (2007).
- [78] R. F. Bishop, E. Buendia, M. F. Flynn, and R. Guardiola, Journal of Physics G: Nuclear and Particle Physics **18**, L21 (1992).
- [79] M. C. Buonaura and S. Sorella, Phys. Rev. B **57**, 11446 (1998).
- [80] N. Trivedi and D. M. Ceperley, Phys. Rev. B **40**, 2737 (1989).
- [81] T. Onogi and S. Doniach, Solid State Communications **98**, 1 (1996), ISSN 0038-1098.
- [82] K. Kim and D. Stroud, Phys. Rev. B **78**, 174517 (2008).
- [83] E. Granato and J. M. Kosterlitz, Phys. Rev. Lett. **65**, 1267 (1990).
- [84] E. Granato, Eur. Phys. J. B **89**, 68 (2016).
- [85] E. Granato, Phys. Rev. B **72**, 104521 (2005).
- [86] K. Efetov, Sov. Phys. - JETP (Engl. Transl.); (United States) .

- [87] A. van Otterlo, K.-H. Wagenblast, R. Fazio, and G. Schön, *Phys. Rev. B* **48**, 3316 (1993).
- [88] S. V. Syzranov, K. B. Efetov, and B. L. Altshuler, *Phys. Rev. Lett.* **103**, 127001 (2009).
- [89] V. Gurarie, L. Pollet, N. V. Prokof'ev, B. V. Svistunov, and M. Troyer, *Phys. Rev. B* **80**, 214519 (2009).
- [90] Y. Kato, Q. Zhou, N. Kawashima, and N. Trivedi, *Nature Physics* **4**, 617 EP (2008).
- [91] R. F. Voss and R. A. Webb, *Phys. Rev. B* **25**, 3446 (1982).
- [92] H. S. J. van der Zant, H. A. Rijken, and J. E. Mooij, *Journal of Low Temperature Physics* **79**, 289 (1990), ISSN 1573-7357.
- [93] F. Couëdo, O. Crauste, A. A. Drillien, V. Humbert, L. Bergé, C. A. Marrache-Kikuchi, and L. Dumoulin, *Scientific Reports* **6**, 35834 EP (2016), article.
- [94] A. Kussmaul, E. S. Hellman, E. H. Hartford, and P. M. Tedrow, *Applied Physics Letters* **63**, 2824 (1993).
- [95] R. B. van Dover, A. de Lozanne, and M. R. Beasley, *Journal of Applied Physics* **52**, 7327 (1981).
- [96] K. K. Likharev, *Rev. Mod. Phys.* **51**, 101 (1979).
- [97] J. Clarke, *Scientific American* **271**, 46 (1994), ISSN 00368733, 19467087.
- [98] R. L. Fagaly, *Review of Scientific Instruments* **77**, 101101 (2006).
- [99] S. L. Sondhi, S. M. Girvin, J. P. Carini, and D. Shahar, *Rev. Mod. Phys.* **69**, 315 (1997).

- [100] J. Kolorenč and L. Mitas, Rep. Prog. Phys **74**, 026502 (2011).
- [101] R. J. Needs, M. D. Towler, N. D. Drummond, and P. L. Ríos **22**, 023201 (2010).
- [102] T. E. Booth and J. E. Gubernatis, Phys. Rev. E **80**, 046704 (2009).
- [103] U. Wolff, Phys. Rev. Lett. **62**, 361 (1989).
- [104] P. A. Whitlock, D. M. Ceperley, G. V. Chester, and M. H. Kalos, Phys. Rev. B **19**, 5598 (1979).
- [105] K. S. Liu, M. H. Kalos, and G. V. Chester, Phys. Rev. A **10**, 303 (1974).
- [106] J. Casulleras and J. Boronat, Phys. Rev. B **52**, 3654 (1995).
- [107] K. J. Runge, Phys. Rev. B **45**, 7229 (1992).
- [108] M. Samaras and C. Hamer, Aust. J. Phys. **52**, 637 (1999).
- [109] E. Granato, Phys. Rev. Lett. **101**, 027004 (2008).
- [110] Y. L. Loh, E. W. Carlson, and K. A. Dahmen, Phys. Rev. B **81**, 224207 (2010).
- [111] X. S. Ling, S. R. Park, B. A. McClain, S. M. Choi, D. C. Dender, and J. W. Lynn, Phys. Rev. Lett. **86**, 712 (2001).
- [112] H. Aubin, C. A. Marrache-Kikuchi, A. Pourret, K. Behnia, L. Bergé, L. Dumoulin, and J. Lesueur, Phys. Rev. B **73**, 094521 (2006).
- [113] D. M. Ceperley, Rev. Mod. Phys. **67**, 279 (1995).
- [114] M. Swanson, Y. L. Loh, M. Randeria, and N. Trivedi, Phys. Rev. X **4**, 021007 (2014).
- [115] N. Cerf and O. C. Martin, Phys. Rev. E **51**, 3679 (1995).

- [116] J. T. Krogel and D. M. Ceperley, *Population Control Bias with Applications to Parallel Diffusion Monte Carlo*, chap. 2, pp. 13–26.
- [117] C. N. Yang, Phys. Rev. **85**, 808 (1952).
- [118] U. Wolff, Phys. Rev. Lett. **62**, 361 (1989).
- [119] N. Metropolis, A. W. Rosenbluth, M. N. Rosenbluth, A. H. Teller, and E. Teller, The Journal of Chemical Physics **21**, 1087 (1953).
- [120] N. Metropolis and S. Ulam, Journal of the American Statistical Association **44**, 335 (1949), pMID: 18139350.
- [121] R. H. Swendsen and J.-S. Wang, Phys. Rev. Lett. **58**, 86 (1987).
- [122] D. Farsal, M. Snina, M. Badia, and M. Bennai, Journal of Superconductivity and Novel Magnetism **30**, 2187 (2017), ISSN 1557-1947.
- [123] K. Binder, Phys. Rev. Lett. **47**, 693 (1981).
- [124] K. Binder and D. Landau, Surface Science **151**, 409 (1985), ISSN 0039-6028.
- [125] K. Binder, Phys. Rev. Lett. **47**, 693 (1981).